

Non-equilibrium ionization and radiative transport in an evolving supernova remnant

Kartick C. Sarkar¹,¹★ Orly Gnat¹ and Amiel Sternberg^{2,3,4}

¹*Racah Institute of Physics, The Hebrew University of Jerusalem, Jerusalem 91904, Israel*

²*School of Physics and Astronomy, Tel Aviv University, Ramat Aviv 69978, Israel*

³*Centre for Computational Astrophysics, Flatiron Institute, 162 5th Avenue, New York, NY 10010, USA*

⁴*Max-Planck-Institut für Extraterrestrische Physik (MPE), Giessenbachstr, D-85748 Garching, Germany*

Accepted 2021 February 25. Received 2021 February 25; in original form 2020 October 2

ABSTRACT

We present numerical simulations of the evolution of a supernova (SN) remnant expanding into a uniform background medium with density $n_{\text{H}} = 1.0 \text{ cm}^{-3}$ and temperature of 10^4 K . We include a dynamically evolving non-equilibrium ionization (NEI) network (consisting of all the ions of H, He, C, N, O, Ne, Mg, Si, S, Fe), frequency dependent radiation transfer (RT), thermal conduction, and a simple dust evolution model, all intra-coupled to each other and to the hydrodynamics. We assume spherical symmetry. Photoionization, radiation losses, photo-heating, charge-exchange heating/cooling, and radiation pressure are calculated on the fly depending on the local radiation field and ion fractions. We find that the dynamics and energetics (but not the emission spectra) of the SN remnants can be well modelled by collisional equilibrium cooling curves even in the absence of non-equilibrium cooling and radiative transport. We find that the effect of precursor ionizing radiation at different stages of SN remnant are dominated by rapid cooling of the shock and differ from steady-state shocks. The predicted column densities of different ions such as N^+ , C^{3+} , and N^{4+} , can be higher by up to several orders of magnitude compared to steady-state shocks. We also present some high-resolution emission spectra that can be compared with the observed remnants to obtain important information about the physical and chemical states of the remnant, as well as constrain the background interstellar medium.

Key words: hydrodynamics – radiative transfer – methods: numerical – ISM: bubbles – H II regions – ISM: supernova remnants.

1 INTRODUCTION

Radiative and mechanical feedback processes from supernovae (SNe) are critical for the evolution of galaxies, influencing small-scale structures and phases states in the interstellar medium (ISM), to global star-formation regulation in galaxy evolution across cosmic time (Larson 1974; McKee & Ostriker 1977; Dekel & Silk 1986; Nath & Trentham 1997; Cox 2005; Breitschwerdt & de Avillez 2006; Krumholz et al. 2018; Dekel et al. 2019). Study of individual and clustered SNe is therefore central for understanding injections of mass, momentum, energy, and metals at $\sim 10 \text{ pc}$ scales, not readily resolved in larger-scale galaxy formation simulations.

Apart from injecting energy, momentum, and metals to the ISM, SN shocks are also important sources of many optical/IR/UV/X-ray emission lines observed in galaxies. A detailed understanding of the emission lines produced in SN remnants (SNRs) is required to distinguish between pure photoionized and shock excited line emissions galactic ISM patches. Most of the existing distinctions are based on different optical line ratios, like $[\text{Si II}]/\text{H}\alpha$, $[\text{O I}]/\text{H}\alpha$, $[\text{O III}]/\text{H}\alpha$, etc. (Mathewson & Clarke 1973; Fesen, Blair & Kirshner 1985; Kewley et al. 2001; Kopsacheili, Zezas & Leonidaki 2020) where shocks are modelled assuming a steady state rather than a complete time-dependent evolution. Optical lines from individual

SNR have also been used to infer the metallicity gradient in an external galaxy or in our Galaxy based on such steady-state models (SSMs; Mathewson & Clarke 1973; Dopita 1976; Dopita, Dodorico & Benvenuti 1980; Fesen et al. 1985; Dopita et al. 2019).

The evolution of individual radiative SNRs has been studied extensively in the literature (McKee & Ostriker 1977; Cioffi, McKee & Bertschinger 1988; Slavin & Cox 1992; Kim & Ostriker 2015; Steinwandel et al. 2020). Although the importance of non-equilibrium ionization (NEI) and cooling was initially neglected, later studies included such complex physics. Hamilton, Sarazin & Chevalier (1983), Kafatos (1973), and Gnat & Sternberg (2007) studied the NEI evolution of different ions for a time-dependent temperature history. Given the temperature history of each cell/particle behind the SNe shocks one can calculate the full ionization dynamics. Self-consistent numerical simulations with NEI networks have also been studied to infer abundances of ions such as O^{5+} , N^{4+} , and Si^{3+} for comparison to observations in the local ISM (Slavin & Cox 1992; De Avillez & Breitschwerdt 2012).

While radiation loss from the SN is important in setting its dynamics, its effect on the ISM and the SN itself has not been studied with proper geometry and time evolution. Attempts have been made to incorporate the radiative transfer along with ionization network. Such attempts, however, remained limited to only steady-state shocks (Shull & McKee 1979; Dopita & Sutherland 1996; Gnat & Sternberg 2009; Sutherland & Dopita 2017) that do not consider either the geometrical factors or the full structure of an

* E-mail: sarkar.kartick@mail.huji.ac.il, kartick.c.sarkar100@gmail.com

SN bubble/remnant. Recently Zhang, Foster & Smith (2018), Zhang et al. (2019), and Steinwandel et al. (2020) studied non-equilibrium chemistry in an SN remnant but they did not include any self-radiation from the SN remnant. In order to overcome such limitations, we for the first time, study the full evolution of an SN structure in a uniform background medium including self-consistent ionization network, radiative transfer, conduction, and a simple evolution of dust.

Our paper is organized as follows. We describe our numerical tools and simulation details in Section 2. We present our results for the dynamics and evolution of SN shock in Section 3. In Section 4, we present our estimations of different column densities and compare them with traditionally used steady-state shock models. A brief discussion of the limitations of our this work is described in Section 5. A summary presented in Section 6.

2 SIMULATION METHOD

We perform spherically symmetric simulations using an NEI network plus radiative transfer (RT) module, described and tested in Sarkar, Sternberg & Gnat (2020, hereafter [paper-I](#)), based on our updated version of the magnetohydrodynamics (MHD) code PLUTO (Mignone et al. 2007). We provide a brief description of our code and the initial set-up in the following sections. We refer the reader to Mignone et al. (2007), Tesileanu, Mignone & Massaglia (2008), and [paper-I](#) for further technical details.

2.1 The code

PLUTO is an Eulerian grid code that uses the finite volume method to solve the fluid equations. The source terms are solved by operator splitting. The full set of hydrodynamics equations are

$$\frac{\partial}{\partial t} \rho + \frac{1}{r^2} \frac{\partial}{\partial r} (r^2 \rho v) = \dot{\rho}_s \quad (1)$$

$$\frac{\partial}{\partial t} (\rho v) + \frac{1}{r^2} \frac{\partial}{\partial r} (r^2 \rho v^2) = -\frac{\partial}{\partial r} p + \rho a_r \quad (2)$$

$$\frac{\partial}{\partial t} E + \frac{1}{r^2} \frac{\partial}{\partial r} [r^2 v (E + p)] = \mathcal{H} - \mathcal{L} + \rho v a_r + \frac{1}{r^2} \frac{\partial}{\partial r} (r^2 F_c) \quad (3)$$

$$\frac{\partial}{\partial t} (\rho X_{k,i}) + \frac{1}{r^2} \frac{\partial}{\partial r} (r^2 v \rho X_{k,i}) = \rho S_{k,i}, \quad (4)$$

where $\rho \equiv \rho(r)$ is the density, $v \equiv v(r)$ is the velocity, $p \equiv p(r)$ is thermal pressure, $E = p/(\gamma - 1) + \rho v^2/2$ is the total energy density, and $\gamma = 5/3$ is the adiabatic index. The source terms, $\dot{\rho}_s$, \mathcal{H} , and \mathcal{L} represent the mass injection rate, thermal heating (via photoionization and charge exchange) and thermal cooling (radiative emissions, recombinations, and charge exchange), respectively. The effect of radiation force on momentum and energy is incorporated by the radiation acceleration term a_r . The conductive flux is given by $F_c = F_{\text{sat}}/(F_{\text{sat}} + |F_{\text{class}}|) \times F_{\text{class}}$, where $F_{\text{class}} = 5.6 \times 10^{-7} T^{5/2} \partial T / \partial r$ erg s⁻¹ cm⁻² (Spitzer 1956) and $F_{\text{sat}} = 5\phi \rho c_{\text{iso}}^3$ with $\phi = 0.3$ (Cowie & McKee 1977).

The ionization network is incorporated through equation (4), where $X_{k,i}$ is the individual ion fraction of element k in its i -th ionization level. The abundances of the elements are kept constant and equal to the Solar values throughout our simulations. The source function, $S_{k,i} = S(X_{k,i-1}, X_{k,i}, X_{k,i+1}, \psi(\mu, v))$ represents the ionization/recombination/photoionization/Auger rates for an ion (k, i) and depends on the local radiation spectra $\psi(\mu = \cos \theta, v)$. This equation therefore is a set of 111 coupled ODEs. The instantaneous

cooling (\mathcal{L}) and heating (\mathcal{H}) functions are calculated based on the local NEQ ion fractions and radiation spectra.

To obtain the local radiation spectra, we solve for the direction dependent specific intensity $\psi(\mu, r, v)$ in a spherically symmetric system by assuming that the change in hydrodynamic or chemical properties in a cell occurs much more slowly than the light traveltime across the system and that the scattering is negligible compared to absorption.¹ The RT equation is then

$$\frac{\mu}{r^2} \frac{\partial}{\partial r} (r^2 \psi(\mu, r, v)) + \frac{1}{r} \frac{\partial}{\partial \mu} ((1 - \mu^2) \psi(\mu, r, v)) = j_v - \alpha_v \psi(\mu, r, v), \quad (5)$$

where $\mu = \cos \theta$ (with θ being the angle between a ray and radial direction), j_v is the isotropic emissivity, α_v is the absorption coefficient (cm⁻¹, which we loosely refer to as *opacity*). Notice that although our system is a 1D spherical system, the solution of a frequency dependent RT equation is a 2D axisymmetric problem.

We also include a simple dust prescription in our simulations. The dust provides extinction (absorption + scattering) and experiences radiation pressure that is assumed to couple instantaneously to the gas. The initial dust properties (extinction cross-section, albedo and average scattering angle) are assumed to be frequency dependent as described by Weingartner & Draine (2001) for $R_v = 3.1$ that is close to the dust properties observed in Milky Way.² The extinction cross-section decreases when the dust is subjected to thermal sputtering (Draine 2011). We assume that the suppression is proportional to a^2 , where $a = 0.1 \mu\text{m}$ is the initial size of a typical dust grain. Although there can be other processes like shattering and evaporation due to shock propagation, the strength of these processes depends on the shock speed that is also represented by the shock temperature. Our dust destruction prescription therefore is very simple and works only to estimate a relative change in the extinction.

A detailed discussion of the techniques and frequencies used can be found in [paper-I](#).

2.2 Initial and boundary condition

Initially, we set the box to have uniform density with hydrogen number density, n_0 at a temperature of $T_{\text{amb}} = 10^4$ K and Solar metallicity. We allow the gas to radiatively cool to a floor temperature of 6×10^3 K. We set the initial ionization state of the medium to collisional equilibrium at $T = T_{\text{amb}}$. The simulation box extends from $r = 0.1$ to 50 pc.

The SN energy is injected by placing $5 M_{\odot}$ of gas with 10^{51} erg of internal energy within a radius of 1 pc at $t = 0$. The inner and outer boundary conditions for the hydrodynamic and chemical quantities are set to an outflow condition, i.e. copied from the inner cells to the ghost zones (no gradient across the boundary). The incoming ($\mu < 0$) radiation spectrum at the outer boundary is assumed to be a uniform Haardt & Madau (2012) background³ for redshift $z = 0$. The inner

¹This is true for most of the frequency range we consider for our RT. One exception is the resonant scattering of Ly α line that requires a better transport solver than presented here. Although the Ly α scattering is, in principle, taken care of by the local emissivity to some extent, the effect only takes place at the next step rather than instantaneously.

²Also available at <https://www.astro.princeton.edu/~draine/dust/dustmix.html>.

³The background radiation does not penetrate more than a few pc from the outer surface due to high absorption cross-section by the neutral hydrogen at our considered densities.

Table 1. List of simulations performed in this paper.

Name	NEI	Self-radiation	Dust	Conduction	Density (H/cm ³)	Resolution (pc)**
CIE*	No	No	No	No	1.0	0.001
NEI	Yes	No	No	No	1.0	0.006, 0.001
NSR	Yes	Yes	No	No	1.0	0.006, 0.001
NSRD	Yes	Yes	Yes	No	1.0	0.006, 0.001
NSRDC	Yes	Yes	Yes	Yes	1.0	0.006, 0.001

* In this case, we assume a plasma in collisional equilibrium.

** In the cases where two resolutions are mentioned, we apply the lower resolution at $r = 0.1$ – 18 pc and the higher resolution at $r = 18$ – 50 pc to resolve the shell better and to lower computational cost. The resolution mentioned here is the default value. We vary this value while checking for convergence with resolution.

boundary condition for the radiation spectrum is set to be reflective i.e. $\psi(\mu \leq 0, \nu) = \psi(\mu \geq 0, \nu)$. This is possible due to the spherical symmetry of the problem.

We perform different simulations with increasing complexity for $n_0 = 1.0 \text{ cm}^{-3}$. First, we assume pure collisional equilibrium for the ionization states of the gas (case, *CIE*). Next, we include the NEI network to calculate the ionization states of the gas on-the-fly (case *NEI*). We include our calculation of self-radiation and couple it to the ionization network in case *NSRD* (short form of non-equilibrium + self-radiation + dust). This case also includes extinction and scattering from dust. Finally, we add thermal conduction along with the ionization network and self-radiation in run *NSRDC* (short form of non-equilibrium + self-radiation + dust + conduction). Although the *NSRD* and *NSRDC* models include a simple prescription of dust evolution, we do not expect the dust to play any major role at $n_0 \lesssim 100 \text{ cm}^{-3}$ (see [paper-1](#)).

Within our 0.1 – 50 pc simulation box, we apply two types of uniform spatial resolution to save computation time. A lower resolution is applied for $r = 0.1$ – 18 pc where the shock is still self-similar ($t \lesssim 23$ kyr) and has not undergone much cooling. A higher resolution is applied for $r = 18$ – 50 pc, where the shock undergoes rapid cooling and shell formation, and is prone to resolution effects. For the case with conduction (*NSRDC*), we apply the high-resolution grids only up to 40 pc (since by 300 kyr, the shock only reaches this point). The grid from 40 – 50 pc is set to have the lower resolution. We sample the angular direction, μ , with 16 uniformly spaced rays between -1 and $+1$ for the purpose of the radiative transfer.

A full list of runs can be found in Table 1. The labels indicate the physics each run includes.

3 CHARACTERISTICS OF A SUPERNOVA

3.1 Different phases

The dynamics of an SN remnant is a very well-studied problem both theoretically and numerically (e.g. Cox 1972b; Cox & Anderson 1982; Cioffi et al. 1988; Kim & Ostriker 2015; Steinwandel et al. 2020). The evolution can be divided into the following phases:

(i) *Free expansion phase*: In this phase, the SN ejecta moves freely through the ISM and the radius of the shock front is, $r_{\text{shock}} = \text{ejecta velocity} \times t$. This happens at $t \lesssim 200 n_0^{-1/3}$ yr, where n_0 is the background hydrogen density (Draine 2011).

(ii) *Sedov–Taylor (ST) phase*: After the end of the free expansion phase, the kinetic energy carried by the SN ejecta is converted into thermal energy by the ISM gas. This energy drives a shock that is self-similar in nature and given by the blast wave solution. At

this stage, $r_{\text{shock}} \propto t^{2/5}$. The observable emission from the earlier part ($\lesssim 5000$ yr) of this phase, however, deviates from a pure CIE plasma and often shows signature of a recombining plasma (Becker et al. 1980; Okon et al. 2019). It is also known that the electron and proton temperatures at this young age of the SN are not equilibrated (Cox 1972a; Itoh 1978; Cui & Cox 1992; Ghavamian, Laming & Rakowski 2007), a feature that we do not model in our simulations. Our estimation of the emission spectrum during the first few 1000 yr is therefore likely inaccurate.

(iii) *Rapid cooling phase*: Since the shock slows down with time ($v_s \propto t^{-3/5}$), the shock temperature decreases and at some point it undergoes thermal instability. At this stage, the shock cools rapidly and radiates away most of its thermal energy over a time-scale of $t_{\text{cool}} \sim 5 \times 10^4 n_0^{-0.55}$ yr (Cox 1972b; Dekel et al. 2019). Although this phase is often considered to be instantaneous, its duration is comparable to the other evolutionary stages (Cox 1972b). Since the physics in this phase has significant consequences on the background material and the shock itself, we put more focus on it. We term the onset of the cooling as $t_{\text{cool,onset}}$ (≈ 20 kyr for $n_0 = 1 \text{ cm}^{-3}$) and the end as $t_{\text{cool,end}}$ (≈ 50 kyr for $n_0 = 1 \text{ cm}^{-3}$). As a result of this rapid cooling, the shock loses its thermal support and collapses to a very thin shell leaving a hot and low density bubble inside. The shell velocity drops temporarily due to the lack of thermal pressure in the shock. We refer to this structure as ‘the shell’ in our discussion.

Although cooling is rapid, the creation of the bubble involves two stages. First, almost 50 per cent of the shocked material (which remains in the outer ~ 6 per cent of the blast-wave) collapses, thus forming a shell. Secondly, the remaining material, mostly within 0.8 – $0.94 r_{\text{shock}}$, cools down at a slightly later time (~ 60 kyr for $n_0 = 1 \text{ cm}^{-3}$) because the density of this material is lower. Once this layer has lost its thermal energy, the hot gas pressure of the bubble pushes it towards the already collapsed shell and forms the final shell. The collapse of these two layers creates additional shock-waves, one of which can be seen moving inwards through the hot and underdense bubble (see upper panel of Fig. 1).

(iv) *Snow-plow (SP) phase*: At $t \gtrsim t_{\text{cool,end}}$, the shell restarts its expansion due to excess pressure from the hot bubble. The expansion of the hot bubble is adiabatic against the background medium, which allows us to estimate the shell radius to be $r_{\text{shock}} \propto t^{2/7}$. This is also the period when the shock temperature is $\lesssim \text{few} \times 10^5$ K and the cooling time behind the shock is so short that it is practically an isothermal shock. This phase of the SN can be seen in emission lines like N II, O III, Si II S II, etc. (Fesen & Kirshner 1980; Ritchey 2020; Ritchey et al. 2020) and is highly susceptible to the effects of NEI and photoionization, a primary focus of this paper. We show the density, temperature, and the hydrogen ionization structure in this phase in Fig. 1.

(v) *Momentum conserving phase*: During the adiabatic expansion, the bubble pressure drops, and at some point falls below the ambient pressure. The shell then enters a momentum driven phase, i.e. $r_{\text{shock}} \propto t^{1/4}$. This phase, however, is not often seen in numerical simulations (Cioffi et al. 1988) before the shell *fades-away*, i.e. the shell velocity becomes equal to the ambient sound or turbulence speeds, at $t_{\text{fade}} \sim 1.9 \text{ Myr } n_0^{-0.37}$ (Dekel et al. 2019).

We run most of our simulations to 300 kyr and therefore capture the ST, rapid-cooling, and SP phases. At later times ($t \gtrsim 300$ kyr), the shell velocity drops below $\approx 40 \text{ km s}^{-1}$ and it is difficult to distinguish the shell from a turbulent ISM. We stress that even though the shell is normally considered to be isothermal in the SP phase, this is not necessarily true in our simulations. The increased pressure due to the accumulation of mass in the shell allows it to expand radially

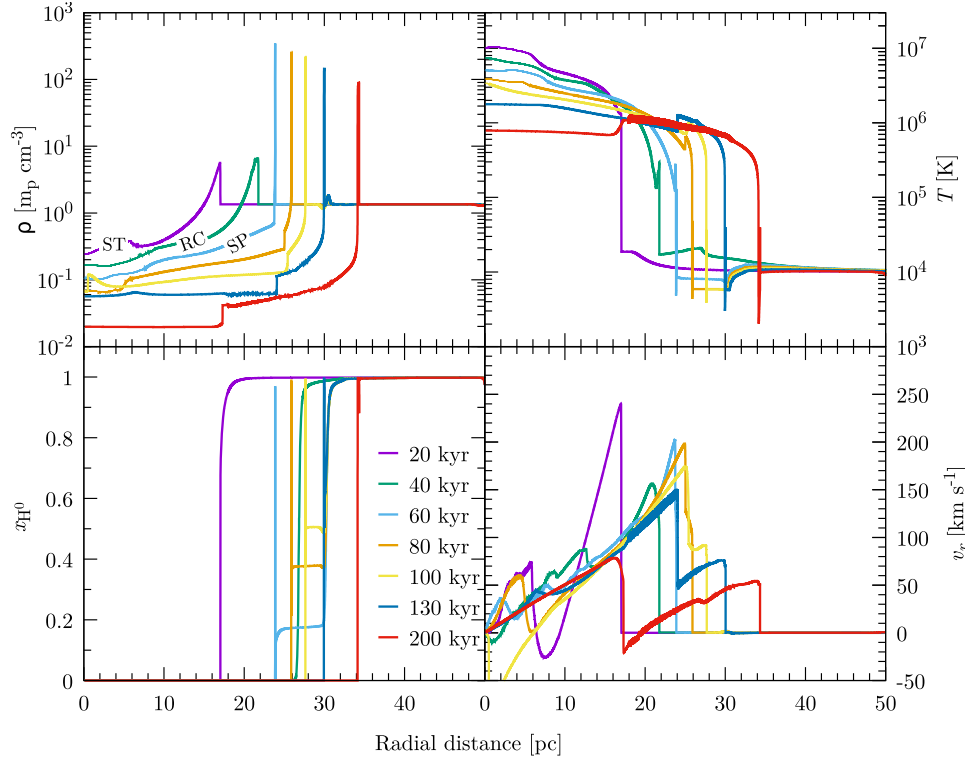


Figure 1. Evolution of density (ρ , top left), temperature (T , top right), Hydrogen ionization fraction (x_{H^0} , bottom left), and radial velocity (v_r , bottom right) structure for the *NSRDC* case (see Table 1). Typical phases of the SN can be seen clearly. The structure is in ST phase at 20 kyr, in rapid cooling (RC) phase at 40 kyr and in SP phase at $t > 60$ kyr. The little bump in front of the shell at $t = 130$ kyr is the stationary ionization front (IF) for all the previous phases. The shell reaches the static IF at $t \sim 130$ kyr.

inwards, reducing the shell temperature below the background level (see temperature plot at $t = 200$ kyr in Fig. 1).

We show the resulting dynamics of our simulations in Fig. 2 for the different physical models. It shows that both the ST and SP phases are broadly similar for all cases (Table 1). Discrepancies, however, appear near the cooling time at ~ 40 kyr as shown in the inset. This is mainly due to varying H and He cooling (mostly by Ly α) at the shock front during the onset at $t_{\text{cool,onset}}$. For *CIE*, the hydrogen fraction, x_{H^0} , follows the temperature and hence $x_{\text{H}^0} \ll 1$ right at the shock front, whereas in *NEI*, hydrogen ionization time-scale delays ionization and hence $x_{\text{H}^0} \approx 0.9$ at the front. This increases cooling at the shock front by a factor of few (see the sharp peaks in Fig. 3), and hence cooling starts affecting the shock much earlier. Introduction of self-radiation reduces this cooling by photoionizing the H^0 ahead of the shock and the dynamics falls back towards the *CIE* case. With the incorporation of thermal conduction the dynamics becomes almost indistinguishable from the *CIE* case. Conduction of heat from the shock front further lowers x_{H^0} and, thereby, decreases early cooling by Ly α . A similar argument also applies for H^0 cooling. We therefore conclude from this discussion that *SN dynamics can be well modelled assuming CIE cooling curves without the inclusion of complex physics like NEI, self-radiation, and conduction*.

It is clear that the ionization precursor is of utmost importance in the dynamics of SN around the cooling time. As can be seen in Fig. 2, the hydrogen IF (r_{if}) moves ahead of r_{shock} at $t \approx 20$ kyr ($t_{\text{cool,onset}}$). This is when the shell starts cooling rapidly and emits in the UV that can ionize the background H^0 gas ahead of the shock. The propagation of r_{if} ends at $t \sim 50$ kyr ($t_{\text{cool,end}}$) when the shell has collapsed completely and radiated away most of its energy. This

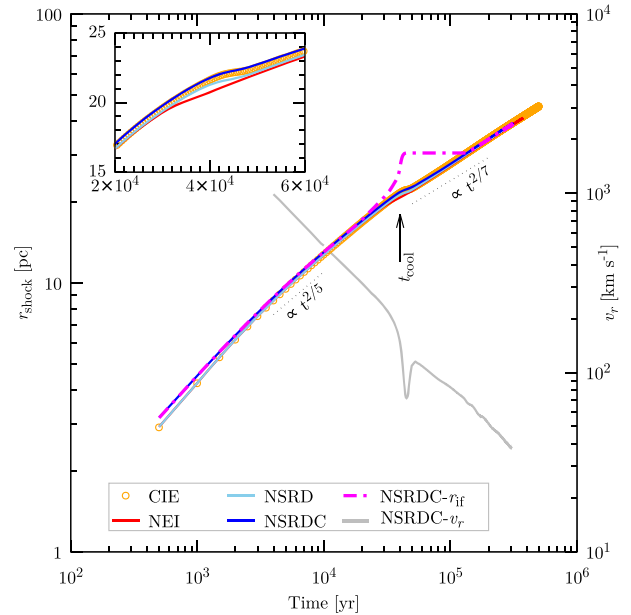


Figure 2. Evolution of shock radius with time for different cases. The cooling time is roughly shown by the vertical arrow. Different line colour shows different cases as described in Table 1. The dash-dotted line shows the IF radius only for *NSRDC* case. The inset shows a zoomed in view of the dynamics around the cooling time. The shock velocity for the *NSRDC* case is shown by the grey solid line for a better understanding of the dynamics.

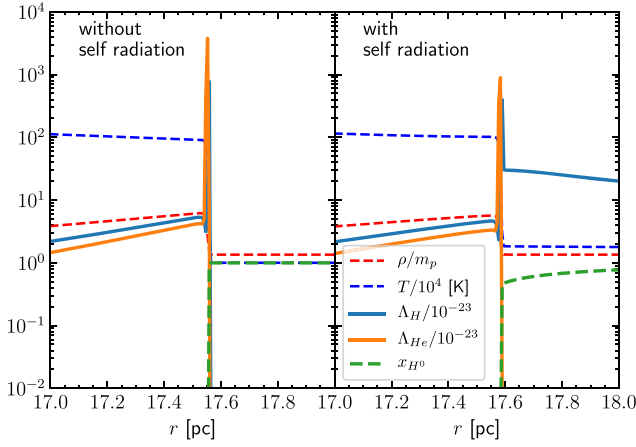


Figure 3. Cooling in the vicinity of shock front at the onset of shell collapse ($t = 23$ kyr) with (right-hand panel) and without (left-hand panel) the self-radiation. Different H^0 and He^0 fractions due to different radiation prescription change the elemental cooling rates (shown in units of 10^{-23} erg $s^{-1} cm^{-3}$).

radius can be calculated by equating the total number of ionizing photons,⁴ $N_{>13.6 eV}$ emitted during this period to the total number of hydrogen atoms to be ionized since the source is short lived compared to the H^+ recombination time, t_{rec,H^+} . The maximum radius of the IF is therefore

$$r_{if,max} = \left(r_{shock}^3 + \frac{3N_{>13.6 eV}}{4\pi n_0} \right)^{1/3}, \quad (6)$$

where we have assumed the emission is from a surface with a radius $r_{shock} = 20$ pc (the shock front at 30 kyr). For our simulation (NSRDC), the total number of emitted hydrogen ionizing photons is $N_{>13.6 eV} \approx 2 \times 10^{60}$. This gives $r_{if,max} \approx 29$ pc which is consistent with the maximum IF radius as seen in Fig. 2. This estimate for the maximum IF radius is only true for atoms with ionizing potentials above 1 Ry. For atoms with lower ionization potential, like C, Mg, Si, S, Fe the IFs can be even larger (depending on the spectrum).

After the IF stops propagating, the ionized hydrogen between r_{shock} and $r_{if,max}$ starts recombining due to the lack of H^0 ionizing photons. The IF, however, does not change its position until it is hit by the shock itself. This happens at $t \sim 130$ kyr when the shell reaches $r_{if,max}$ and the velocity of the shell is ~ 70 km s^{-1} . By this time, the velocity of the shock-induced IF is smaller than the shock velocity, and a stable radiative-precursor therefore no longer exists. Rather the material that has been ionized at earlier stages lingers ahead of the shock, because it has not yet recombined, and creates an effective ionized precursor to the shock.

⁴The integration of total ionizing photons is done during 22–50 kyr period. Since part of the photons with energy >13.6 eV is also going to get absorbed by H^0 , the available H^0 ionizing photons = photons(>13.6 eV) – photons(>24.6 eV) + $0.2 \times$ photons(>24.6 eV). Here, 0.2 is the assumed fraction of photons with energy >24.6 eV emitted due to direct recombination of He^+ to He^0 ground state (Draine 2011). Notice that this is only ~ 5 per cent of ionizing photons if we assume that all the SN energy is emitted in LyC photons. Just to compare, the total amount of radiated energy in the rapid cooling phase is ~ 30 per cent of the SN energy (Fig. A1). Therefore, most of the radiation in this phase is radiated at energies <13.6 eV.

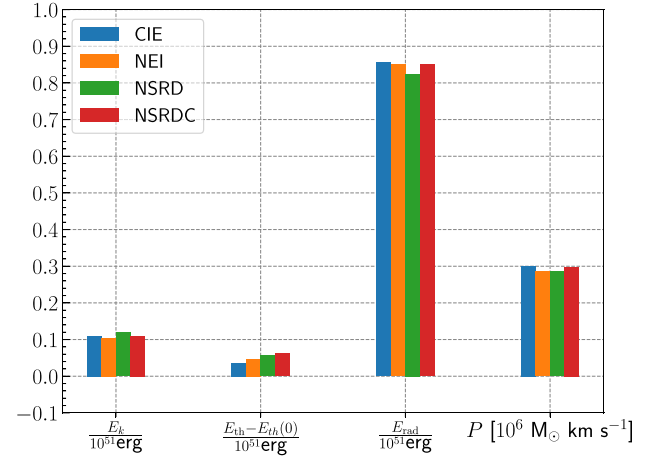


Figure 4. Energetics of an SN in a $n_0 = 1$ cm $^{-3}$ background medium at the end of the simulation, i.e. $t = 300$ kyr. Simulations containing different physics are shown by different colours. From left to right are the kinetic energy, net gain in thermal energy in the box, radiation loss, and total momentum in the simulation box.

3.2 Energetics

As has been discussed many times in the literature, the key quantities to know in order to incorporate SN physics in galaxy formation and evolution simulations are the thermal energy, kinetic energy, and momentum injection rates for SNe. Therefore, in Fig. 4, we plot the total thermal energy and momentum deposited in each case (Table 1) at the end of the simulation i.e. 300 kyr. At this time, the energetics becomes almost constant (see Fig. A1 in the Appendix) and varies by only a few per cent with time. Fig. 4 shows that 80–85 per cent of the SN energy is lost by radiation. The second column represents the change in the total thermal energy inside the box and shows that only ~ 5 per cent of the SN energy is retained as thermal energy of the box. This value goes down further by few per cent as time evolves further. The total kinetic energy and momentum retained in the box are about $\sim 10^{50}$ erg and $2.8\text{--}3.0 \times 10^5 M_\odot$ km s^{-1} , respectively. These numbers are fully consistent with other previous estimates, e.g. Kim & Ostriker (2015). It is therefore clear that the incorporation of the complex physics like NEI or radiative transfer does not change the resulting energetics from the values obtained by simple CIE simulations by more than a few per cent.

3.3 Cooling function

As far as the cooling is concerned, it has been suggested that traditional cooling curves obtained from 0-dimensional non-equilibrium isochoric calculations can be used as a supplement, instead of the actual ionization network in more complex hydrodynamic simulations (de Avillez & Mac Low 2002; Vasiliev 2013). In an attempt to understand the working cooling curve behind the shock, we plot the cooling function ($\Lambda/n_e n_H$ erg $s^{-1} cm^3$) of the shell region (from r_{bub} to r_{shock})⁵ in Fig. 5. The figure also depicts a time evolution of the cooling function, the first ~ 5 kyr of which is probably affected by the electron–ion non-equilibrium and therefore has not been shown

⁵The bubble radius is defined to be the radius where the density crosses a certain threshold while going from the centre. This critical value $\geq 0.5n_0$ during ST phase and $\geq 5n_0$ during the snow plow-phase to consider a sufficient region of shocked gas but to avoid including the bubble.

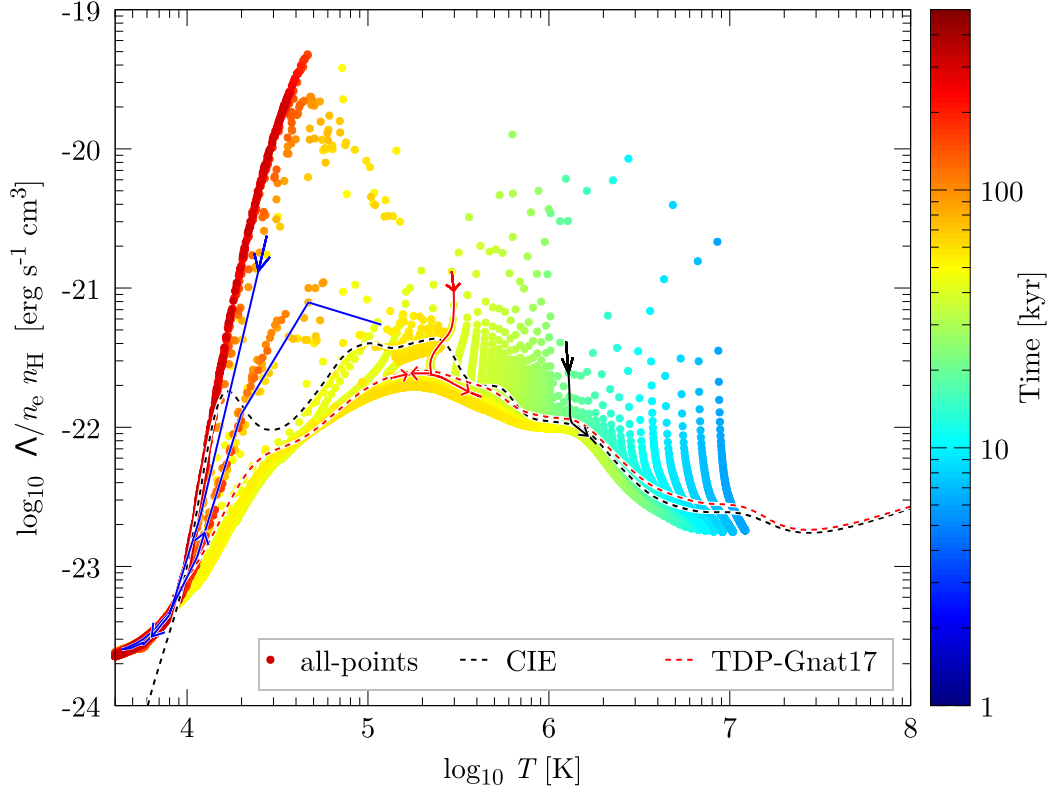


Figure 5. Cooling function in the region between r_{shock} and r_{bub} at all times. Time is shown by the colour of each point. Typical spatial tracks at 20 kyr (representing ST phase), 40 kyr (rapid cooling phase), and 80 kyr (SP phase) are shown by black, red, and blue arrows, respectively. These cooling functions have been compared with more traditional cooling curves. We have not intentionally plotted the points for $t < 5$ kyr since electron temperature may not follow the proton temperature at such early times.

in the plot. We also show two other traditional cooling curves, one for CIE (Gnat & Sternberg 2007) and the other is for time-dependent isochoric cooling in the presence of photoionization (Gnat 2017) for comparison. The figure shows large variations in the cooling functions where it does not follow any known cooling curves. At early times (in the ST phase, $t \lesssim t_{\text{cool,onset}}$, green shades) most of the points, however, are concentrated on the CIE cooling curve. This is also demonstrated by the black arrows, which represent a spatial track at 20 kyr, starting from r_{shock} to r_{bub} . One can think of this spatial track as the evolution of a single lagrangian cell of gas after it is shocked, and as it flows away from the shock. As the track shows, the cooling for the first few points just behind the shock front is much higher than for CIE and indicates that the plasma is underionized. During the rapid cooling phase ($t_{\text{cool,onset}} - t_{\text{cool,end}}$, orange shades), this curve behaves like a time-dependent photoionized plasma (although with a different radiation field). This is shown by the yellow points and corresponding spatial track (red arrows). This is due to the highly radiative shell that emits sufficient ionizing photons to keep the whole shell close to ionization equilibrium. The upturn of the arrow towards the end of the spatial track at 80 kyr represents the bubble-shell interface where temperature rises and the cooling tends to behave like a CIE one. In the SP phase ($t \gtrsim 60$ kyr, shown using reddish shades), the cooling curve does not follow the traditional curves and rather evolves in a more vertical way. As can be seen in the example track at $t = 80$ kyr (blue arrows), the cooling at the shock front is almost an order of magnitude larger than at CIE. The cooling, however, soon settles down to the CIE values. Below $T \lesssim 10^4$ K, the CIE curve drops sharply due to the absence

of any atomic coolant but in the presence of radiation, very tiny amount of ionized H and metals keeps the cooling higher. At even later times ($t \gtrsim 200$ kyr), cooling occurs mostly in simple vertical streak at $\sim 2 \times 10^4$ K where the cooling just behind the shock can be almost two orders of magnitude higher than the CIE one. This difference in cooling in the SP phase, however, does not change the dynamics of the shell, since at this point, the shell is mainly driven by the hot pressure of bubble and not the thermal energy of the shell.

3.4 Radiative transfer in shell

To understand the nature of precursor ionization, we show the ionizing photon luminosity ($Q = 4\pi r^2 \Phi$ with $\Phi =$ radial photon flux in $\text{cm}^{-2} \text{s}^{-1}$) from the remnant in Fig. 6. We plot the ionizing photon luminosity for H ionizing ($E > 13.6$ eV) and He ionizing ($E > 24.6$ eV) photons just outside the shock front $r = r_{\text{shock}} + \Delta r$ (numerically, the next cell) and at the bubble-shell interface $r = r_{\text{bub}}$. As can be seen in the figure, both Q_{H} and Q_{He} rise slowly until $t = t_{\text{cool,end}}$ and then drop sharply after most of the thermal energy in the shock is radiated away. Prior to $t_{\text{cool,onset}}$, the photons are mainly He ionizing but the photons are mostly H ionizing from $t_{\text{cool,onset}}$ to $t_{\text{cool,end}}$. This is also the period when the IF detaches from the shock front and pre-ionizes the background material.

The photon luminosities and signs (ingoing or outgoing) at r_{bub} ($Q_{\text{H,bub}}$ and $Q_{\text{He,bub}}$) provide an inside view of what is happening at the shock. Let us define a positive luminosity as a net outflux

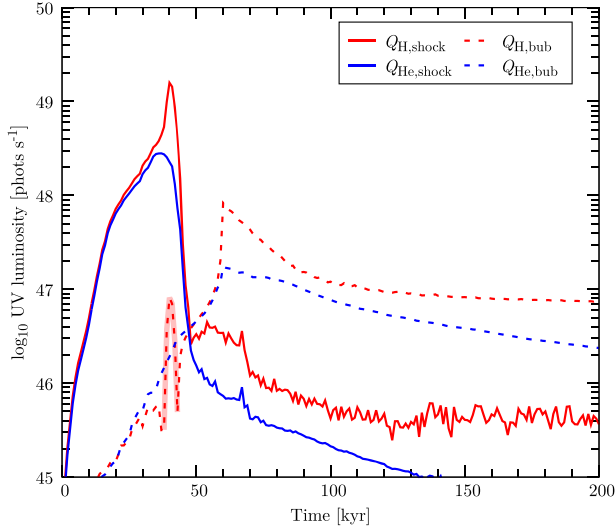


Figure 6. Radial flux of H^0 ionizing (Q_H) and He^0 ionizing (Q_{He}) photons at the shock front (r_{shock}) and at the shell-bubble interface (r_{bub}). Instances where $Q_H < Q_{He}$ mean that there was net radial influx of photons. The shaded part of the curve at $t \sim 40$ kyr is where $Q_{H,bub} < 0$ (indicating net influx) and only the absolute value has been plotted to show the values.

of photons and a negative luminosity as a net influx of photons. The negative luminosity (shaded pink in the background) in $Q_{H,bub}$ between $t_{cool,onset}$ and $t_{cool,end}$ therefore means that there is a net influx of photons during this phase due to the extremely bright cooling shell. After $t_{cool,end}$, the bubble luminosity increases slowly and finally rises above the shock luminosity at $t \approx 45$ kyr signifying negligible emission from the shell. It is clear that the shock luminosity is much smaller than the bubble luminosity at all later times. This means that even if the bubble is emitting some ionizing photons, they are absorbed by the dense shell and only a very small fraction of the ionizing photons escape. The escape fraction (f_{esc}) of such photons from the shell depends on the time and is ~ 10 per cent for the LyC photons. The escape of He ionizing photons is even smaller, of the order of few per cent.

3.5 Ionization precursor

Understanding the ionization precursor has been at the centre of modelling the emission from shocks. From the pioneering work of Cox (1972a) to later works by Shull & McKee (1979), Dopita (1976), Gnat & Sternberg (2009), and Sutherland & Dopita (2017) all focused on modelling the ionization precursor from a plane-parallel shock with a given steady-state velocity. Such models are good for shocks that have already entered the steady state in a background medium that is not affected by anything other than the shock itself. This is certainly not the case for an SN which undergoes different phases (see Section 3.1) and is hardly in steady state. We therefore present the full evolution of the ionizing photon fluxes and H, He ion fractions just in front of the shock (numerically, we choose this to be the cell immediately next to the shock front). A useful parameter in this context is the ionization parameter, $U = \Phi/n_0 v_s$, where Φ is the photon flux and v_s is the shock velocity. This ratio compares the number of available ionizing photons to the incoming flux of neutral gas that needs to be ionized to create a precursor. This means that (i) for shocks with $U \ll 1$, the gas ahead of the shock will be only slightly ionized, and only close to the shock front (ii) for shocks

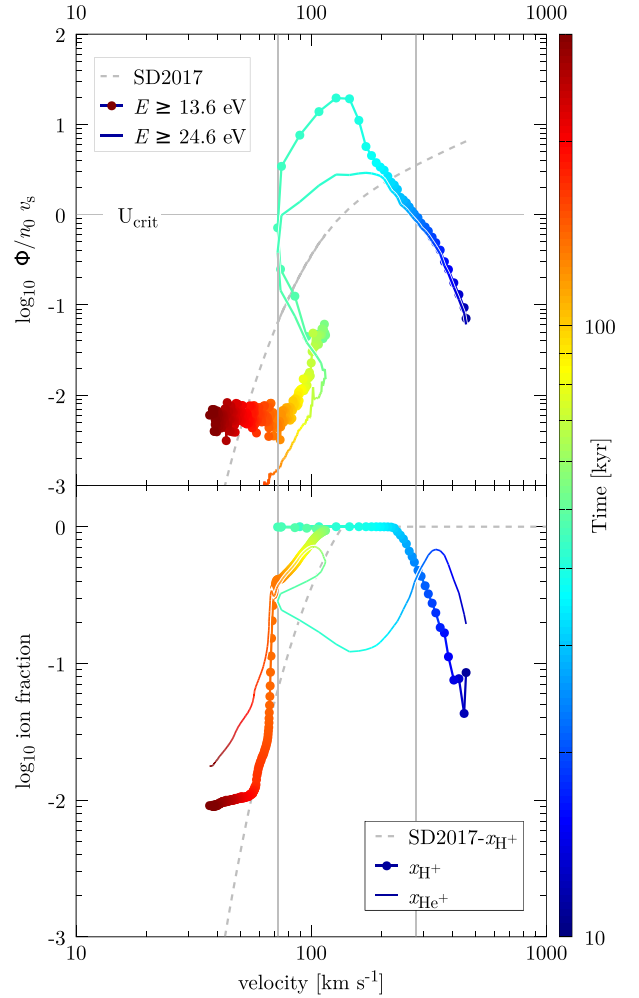


Figure 7. *Upper panel:* Ionization parameter $U = \Phi/n_0 v_s$ as a function of shock velocity, v_s . Colour shows time from the onset of SN. The blue, cyan, and reddish part of the curves roughly represent the ST, rapid cooling phase, and SP phase, respectively. The dashed grey line represents the ionization parameter calculated by Sutherland & Dopita (2017, SD2017; their equation 31). The horizontal bar shows $U = U_{crit} = 1$ and the vertical lines show the corresponding velocities. *Bottom panel:* H^+ and He^+ ionization fractions as a function of velocity and time. The dashed grey line shows the calculation from SD2017. The non-monotonous behaviour of the simulated curves with velocity is due to the non-monotonous behaviour of the shock velocity itself during the rapid cooling phase since it stalls temporarily and then restarts again.

with $U \lesssim 1$, the precursor will have noticeable ionized gas but there will still not be any IF, and (iii) for $U > 1$, the precursor will be fully ionized and an IF will run ahead of the shock front, forming a radiative-precursor. We term this critical value of the ionization parameter as U_{crit} .

The ionization parameter for our NSRDC simulation is plotted in Fig. 7 as a function of velocity for a comparison to steady-state calculations. Since the shock velocity in the SN remnant decreases over time, it is easier to read the figure from right to left and then to compare it with SSMs. As can be seen in the upper panel of the figure, U initially rises with decreasing velocity due to the decrease in shock temperature and hence increase in overall cooling rate that increases the shell luminosity. In addition, the decreasing temperature of the shock lowers the average energy of the emitted photons (compared

to X-ray photons earlier) so that the number of ionizing photons increases. It crosses $U = 1$ at a velocity of $\approx 280 \text{ km s}^{-1}$, at a time of $t_{\text{cool,onset}}$. Note that the main difference between our results and the SSMs at this stage is purely due to the non-steady-state nature of the our shocks. Between $t_{\text{cool,onset}}$ and $t_{\text{cool,end}}$ (corresponding a velocity of $280\text{--}70 \text{ km s}^{-1}$), $U \gg 1$ and the radiative-precursor IF reaches $r_{\text{if,max}}$ (see Fig. 2).

After $t_{\text{cool,end}}$ (at a velocity $\lesssim 70 \text{ km s}^{-1}$), U drops sharply to $U \approx 10^{-1}$ due to the absence of any photon production from the shell (also seen in Fig. 6). The shock finally reaches a steady state at $t \gtrsim 70 \text{ kyr}$ with a velocity $\lesssim 115 \text{ km s}^{-1}$.⁶ Although $U \ll 1$ at this stage, the gas ahead of the shock is still slightly ionized, though the ionization fraction is decreasing with time and velocity (see the lower panel of this figure as well as Fig. 1). This is because the shock is still inside the ionized sphere ($r_{\text{shock}} < r_{\text{if,max}}$) created by the rapid cooling phase of the SN, which has not yet recombined.

The hydrogen ionization fraction (x_{H^+}) finally drops to very low value only at velocities $\lesssim 70 \text{ km s}^{-1}$ when $r_{\text{shock}} = r_{\text{if,max}}$. From this point onward, the background can be considered truly unperturbed. It is an interesting coincidence that this velocity (70 km s^{-1}) is also the limit found by for SSMs below which even a partially ionized precursor cannot be present (Shull & McKee 1979; Sutherland & Dopita 2017). While our results agree, we differ in physical explanations of this phenomena for a cooling SN shock. In steady-state shock models, the precursor is created by photons emitted by the down-streaming material, the characteristics of which depends on the shock velocity. In our evolving-SN shock model, the precursor is put in place during the rapid cooling phase and is independent of the shock velocity afterwards.

The evolution shown in this plot can be divided into four parts. Initially ($v \gtrsim 300 \text{ km s}^{-1}$), the ionization parameter and ionization fraction in our evolving shocks are considerably lower than those obtained in the SSMs. This is because our young shocks have only gone through a limited spatial extent, much smaller than the cooling length of the gas. The emitted radiation, which is proportional to the shocked-material depth, is hence much smaller. Later, for $130 \lesssim v \lesssim 300 \text{ km s}^{-1}$, both the SSMs and our evolving shocks agree that the ionization parameter and ionized fraction are significant, although they differ in detail. At even lower velocities ($70 \lesssim v \lesssim 130 \text{ km s}^{-1}$), the SSMs predict that the up-streaming material should only be partially ionized and no fully ionized precursor should form⁷ (Sutherland & Dopita 2017). In our models, however, a layer of ionized material still precedes the shock front. This material has been ionized during the rapid cooling phase, and has not yet recombined. As is shown by the grey dashed line in the bottom panel of Fig. 7, that the H^+ ionization fraction produced in this way is larger than the expected fraction from a plane-parallel steady-state shock at this velocity range. Finally, for shock velocities below 70 km s^{-1} , the ionization ahead of the shock drops in our evolving models as well and at $60 \lesssim v \lesssim 70 \text{ km s}^{-1}$, the ionization fraction is consistent with the expected values from the SSMs. Below $v \lesssim 60 \text{ km s}^{-1}$,

the ionization fraction in our simulation is mostly reminiscent of the initial 10^4 K ambient gas. *In conclusion, the applicability of SSMs to the SNRs is therefore quite limited.*

4 OBSERVABLES

We now turn our attention to some of the observable properties of SNRs that show the importance of these inter-playing physical processes.

4.1 Column densities

Ionic column densities are related to the intensities of emission or absorption lines. For steady state planar shocks, the column densities are functions of velocities. However, as we have discussed earlier, the expanding SN shock is not in a steady state.

Fig. 8 shows the behaviour of example ions near the shock. We focus on N^+ , N^{2+} , and N^{4+} as our examples. Other ions with similar ionization energies follow similar trends. For example, N^+ , O^+ , S^+ behave as N^+ . The ions like N^{2+} and O^{2+} follow N^{2+} , and ions like O^{5+} follow the N^{4+} trends. In each panel, we show the temperature, T (red solid line), the N^+ ion fraction, x_{N^+} (blue dashed line), and the N^+ cumulative column density, N_{N^+} (blue solid line). Similarly, we show $x_{\text{N}^{2+}}$ (brown dashed), $N_{\text{N}^{2+}}$ (brown solid), $x_{\text{N}^{4+}}$ (green dashed), and $N_{\text{N}^{4+}}$ (green solid). The different rows show simulation results for our four model runs *CIE*, *NEI*, *NSRD*, and *NSRDC*. The columns are snapshots at various phases. The left most column, at $t \sim 20 \text{ kyr}$, represents the ST phase when the SN evolution is purely self-similar and the temperatures are high enough for the ions behind the shock front (not at the shock front though) to follow collisional equilibrium. Secondly, at $t \sim 40 \text{ kyr}$, the shell is in the rapid cooling phase, cooling down to temperatures where NEI comes into play. Thirdly, at $t \sim 80 \text{ kyr}$, the shock is isothermal, but the radiation from the rapid cooling phase is still dominating the precursor ionization. And fourthly, at $t \sim 160 \text{ kyr}$, the shock is still isothermal but the ionization precursor has disappeared. As we discussed in Section 3.1, the inclusion of different physical ingredients leads to earlier or later cooling and therefore slightly different shock radii as can be seen in the figure.

4.1.1 Origin of ions

Fig. 8 shows that most of the N^+ column density in the ST phase comes from the background, which is either collisionally ionized or slightly photoionized due to the radiation from the shock. At later stages, the region immediately behind the shock-front also contributes to N^+ column. This is because the shock temperature is $\sim \text{few} \times 10^4 \text{ K}$ and suitable for N^+ production at later times ($t > t_{\text{cool}}$). Assuming *CIE*, x_{N^+} follows the temperature. Therefore, it is large only at the shock front, at the inner boundary of the relaxation layer⁸ and at the bubble-shell interface where the temperature is suitable to produce N^+ . However, the contribution of the bubble-shell interface to the cumulative column density N_{N^+} is negligible.

For *NEI*, because the $\text{N}^+ \rightarrow \text{N}^0$ recombination time is longer than the cooling time of the shock, x_{N^+} does not immediately fall to zero inside the shell. Since the density of the shell is very high, even a

⁶Recall that the shock velocity increases from 70 km s^{-1} at $t \approx 50 \text{ kyr}$ to 115 km s^{-1} at $t \approx 60 \text{ kyr}$ due to re-acceleration of the shock after the shell stalls temporarily (Fig. 2).

⁷Note that by ‘precursor’ we refer to a steady ionization layer that runs ahead of the shock, such as, occurs when the IF velocity is larger than the shock velocity. For lower velocities, photoionization could still occur, but it is limited to the immediate vicinity of the shock front. In this case, the gas may enter the shock ionized, even though a stable precursor does not form. We note that other works do not make this distinction, and refer to both cases by the name ‘precursor’.

⁸The relaxation layer is defined, in an isothermal shock, to be the layer from the shock front where the gas is just shocked and does not have enough time to cool to the background temperature. The thickness of this layer is roughly $v_s \times$ the cooling time of the shocked gas.

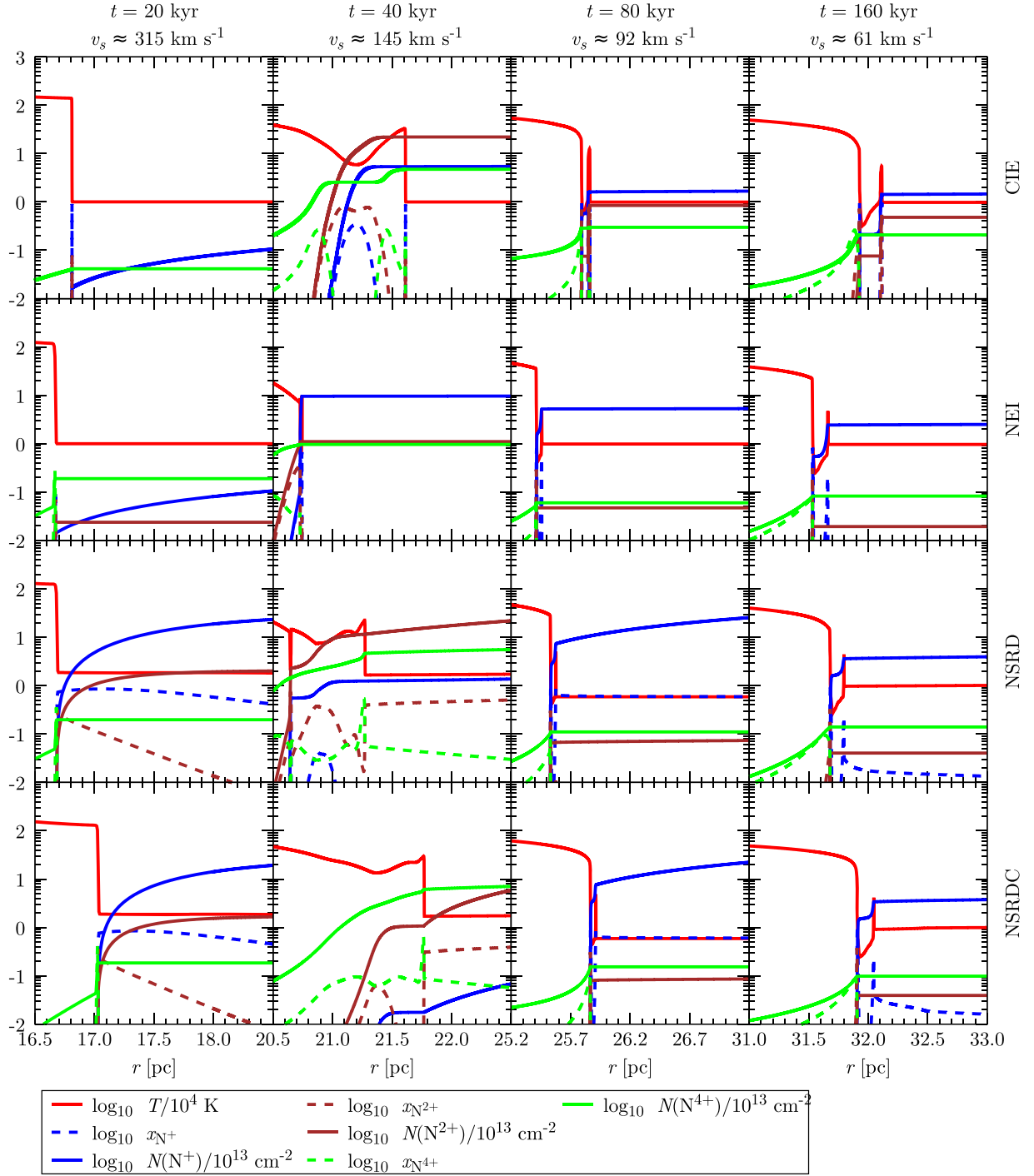


Figure 8. The behaviour of the Nitrogen ions, N^+ , N^{2+} , and N^{4+} , near the shock front $r = r_{\text{shock}}$ for the four model runs with the differing physical processes (rows, legend on the right-hand side) at four snapshots in the SN evolution (columns). The first, second, and third columns represent the ST, rapid cooling, and SP phases, respectively. The fourth column is for a late time at which the ionization precursor has vanished. The solid-red, and the blue, brown, and green dashed lines show, respectively, the temperature of the fluid, and the x_{N^+} , $x_{\text{N}^{2+}}$, and $x_{\text{N}^{4+}}$ ion fractions. The corresponding solid lines show the cumulative column densities, $N(< r)$ (in units 10^{13} cm^{-2}), for the three Nitrogen ions.

small N^+ fraction in the shell can produce a significant N_{N^+} . This is the main difference between the *CIE* and *NEI* column densities.

The introduction of self-radiation in *NSRD* increases x_{N^+} in the shell as well as in the up-streaming material by pre-ionizing it. However, the main difference is the presence of N^+ in the up-streaming

material. This difference between *NEI* and *NSRD* reduces to only a factor of ~ 2 at $t \gtrsim 130 \text{ kyr}$ (see Section 4.1.2) when the shock reaches the H-ionization front, $r_{\text{if,max}}$ but leaves a trace amount of N^+ at larger radii which is still recombining. In addition, since the velocity falls below $\sim 70 \text{ km s}^{-1}$, it is also not able to create a precursor by itself.

Introduction of conduction in *NSRDC* does not change the qualitative picture much from the *NSRD* case, at least for N^+ .

Intermediate ions like N^{2+} are mainly generated either at the shock front or in the precursor region during the ST phase. For the *CIE* and *NEI* cases, most of the N^{2+} column remains small and originates in the shock-front, whereas in the *NSRD* and *NSRDC* cases, the radiation from the shock (which is mostly He ionizing before $t < t_{\text{cool,onset}}$) pre-ionizes the upstream material to produce N^{2+} . At later times $t \gtrsim 80$ kyr, the contribution from the shock front can be significant for the *CIE* case. For the cases with non-equilibrium network, the contribution from the shock front is negligible due to the long ionization time-scale for the $N^+ \rightarrow N^{2+}$ transition, and most of the N^{2+} column is formed in the bubble-shell interface. Since the size of this interface and the density and temperature structure at the interface is sensitive to the resolution, this introduces convergence issues for the intermediate ions. We discuss this further in Section 4.1.3. At still later times ($t \gtrsim 250$ kyr; see Fig. A2) the outer region of the bubble cools down to below 10^5 K and becomes the dominant contributor.

Higher ions like N^{4+} and O^{5+} originate mainly from the self-similar region in the ST phase for the *CIE* case, but from the shock front for the non-equilibrium cases. This is due to the long ionization time-scale for $N^{4+} \rightarrow N^{5+}$. A substantially higher column density ($\sim 10^{14} \text{ cm}^{-2}$) of N^{4+} can be observed during the rapid cooling phase when the shell density is higher and the temperature is in the suitable range. The column density decreases in the SP phase for *CIE*. The main contribution to highly ionized gas then comes from the hot bubble where the temperature is suitable to produce these ions. The introduction of the non-equilibrium effects delays recombination of highly ionized gas (for example, $N^{6+} \rightarrow N^{5+}$, or $O^{7+} \rightarrow O^{6+}$) and hence decreases the ion fractions of the lower ions too. This delayed recombination also reduces the total cooling rate of the hot gas inside the bubble (where $10^5 \lesssim T \lesssim 10^6$ K in Fig. 8). As a result, the bubble temperature is generally higher in the *NEI* case compared to *CIE*. Self-radiation does not affect the higher ions, as the ionization potentials are much larger than the average photon energy emitted in the SP phase. This is because the shock temperature in this phase is only a few $\times 10^4$ K.

The introduction of conduction helps to decrease the bubble temperature by transferring energy to the shell, and thereby slightly increases the recombination rates in the bubble. This causes the N^{4+} fraction and column to increase compared to the no-conduction cases. This increase in the higher ion column densities, however, is not comparable to the peak achieved during the rapid cooling phase. The higher ions like C^{3+} , N^{4+} , and O^{5+} can have column densities $\gtrsim 10^{14} \text{ cm}^{-2}$ (for $n_0 = 1 \text{ cm}^{-3}$ case) during this phase. An example of such peaks can be seen in Fig. 9. *Therefore, observations of these ions in excess of $\sim 10^{14} \text{ cm}^{-2}$ may indicate a rapid cooling phase of the SN remnant.*

4.1.2 Time evolution of column densities

Fig. 9 shows the evolution of column densities (integrated from the centre to the edge of the simulation box) as a function of time. The different curves show the behaviour for our four simulation runs. They all start with an initial N^+ column density (left-hand panel) of $\approx 2 \times 10^{13} \text{ cm}^{-2}$ corresponding to the initial set-up of box size of 50 pc, density $n_0 = 1 \text{ cm}^{-3}$ and temperature of 10^4 K. In the *CIE* and *NEI* cases, N^+ starts to fall as the background material cools down and recombines over time. The column density jumps suddenly at $t \sim t_{\text{cool}}$ due to the rapid cooling phase where the temperature of

the whole cooling shell is $\sim \text{few} \times 10^4$ K, appropriate for the N^+ production. The column density decreases at $t \gtrsim t_{\text{cool}}$ kyr due to a low shell temperature ($\approx 10^4$ K) and the only contribution from the shock comes from the relaxation layer. In *CIE*, this contribution keeps the total N^+ column density slightly higher than the background level. The shell, in the *NEI* case, contributes slightly more due to delayed recombination of N^+ .

The introduction of radiation has an immense effect on the N^+ column at $t \lesssim 130$ kyr ($v_s \gtrsim 70 \text{ km s}^{-1}$). During the ST phase ($t \lesssim t_{\text{cool,onset}}$), the He ionizing radiation can also ionize N^0 to N^+ even before the H-ionization front runs ahead of the shock. As explained in the previous section too, most of the N^+ column density comes from this precursor region although the contribution from the precursor decreases at $t \gtrsim t_{\text{cool}}$ since N^+ recombines with time and finally vanishes at $t \sim 130$ kyr when the shock reaches the H-ionization front. After this point, the main contribution to the N^+ column comes from the delayed recombination at the shock front and the trace amount of N^+ in the background.

The slight dip in N_{N^+} at $t \approx t_{\text{cool}}$ happens due to the high number of ionizing photons originating from the rapid cooling phase that ionizes $N^+ \rightarrow N^{2+}$. This explains why the N^{2+} column (middle panel) peaks rapidly at $t \approx t_{\text{cool}}$. Note that the peak for the cases with self-radiation is much higher compared to the normal peak (due to rapid cooling phase) for the cases that do not have radiation (*CIE* and *NEI*). Once the shell cools down completely, the only contribution to the N^{2+} column comes from the forward shock. As can be seen in Fig. 8 the shock temperature in the *CIE* run is higher than for the non-equilibrium cases. This is because of the underionized plasma that increases the cooling efficiency at the shock front as can be understood from Figs 3 and 5. Therefore, the shock temperatures in the non-equilibrium cases do not reach $\sim 10^5$ K required for N^{2+} production at $t \gtrsim t_{\text{cool}}$. This is why $N_{N^{2+}}$ in the *CIE* case is much higher than in the non-equilibrium cases. For the non-equilibrium cases, the main contribution to the N^{2+} column comes from the bubble-shell interface at $t_{\text{cool}} \lesssim t \lesssim 200$ kyr. At $t \gtrsim 200$ kyr, the bubble temperature decreases to $\sim 10^5$ K due to adiabatic expansion and becomes the main source of N^{2+} column.

It is clear that the peak in column density at $t \sim t_{\text{cool}}$ is a general feature since the shell cools rapidly due to thermal instability and passes through all the temperature zones, thereby producing peaks in all the ion columns. The higher the ionization potential, the earlier an ion peak appears for (as can also be seen in Fig. 9).

Although the behaviour for N^{4+} is similar to N^{2+} , in the sense of a rise to a peak and then a decline, there are some key differences before and after the cooling of the shock. In the ST phase, the N^{4+} column for the *CIE* run is mainly driven by the presence of a small fraction of N^{4+} in the whole self-similar region. On the other hand, in the non-equilibrium cases there are contributions from the self-similar region and also from a thin region at the shock front where the temperature is suitable for N^{4+} production. This layer is broader in the non-equilibrium cases due to the ionization time-scale for $N^{3+} \rightarrow N^{4+}$. This leads to a larger N^{4+} column even in the ST phase for the non-equilibrium cases. After $t \gtrsim t_{\text{cool}}$, the temperature in the bubble becomes suitable for N^{4+} production and therefore becomes the main source of N^{4+} . The non-equilibrium cases, on the other hand, contain a low ionization fraction, $x_{N^{4+}}$, due to the delayed recombination time of higher ions as explained in Section 4.1.1. Conduction at the shell-bubble interface helps transfer extra heat from the bubble to the shell and mass from the shell to the bubble, thereby increasing the recombination rate of highly ionized nitrogen. The actual amount of N^{4+} contribution from the bubble, however, depends on the exact temperature and density values of the bubble at any time, since

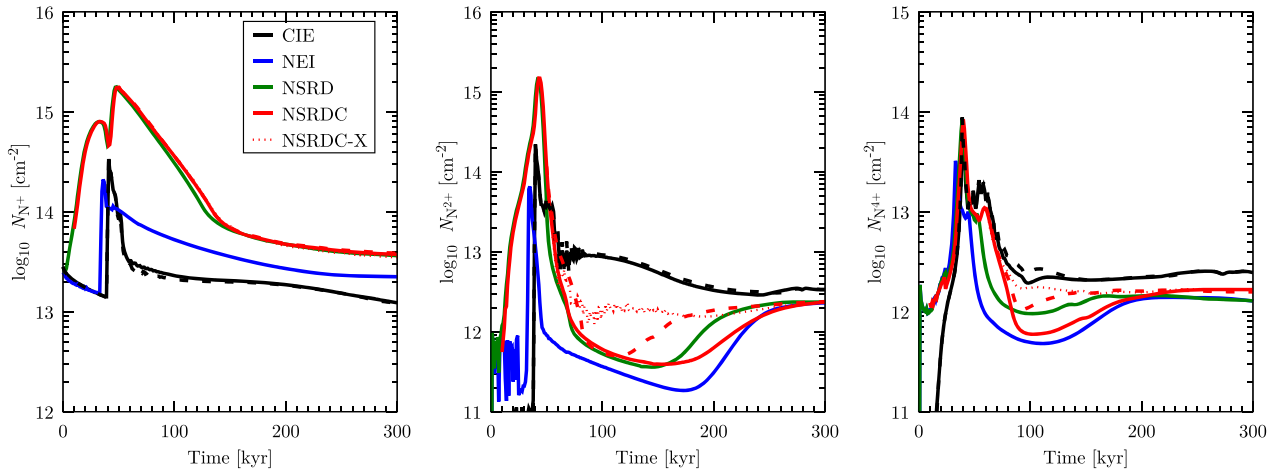


Figure 9. Time evolution of N^+ , N^{2+} , and N^{4+} column densities from the simulation box. Different cases are shown by different colours. The origin of the double-hump structure in $N_{N^{4+}}$ is due to the two stage collapse of the shell during the rapid cooling phase as described in Section 3.1. The magnitude of the second hump is smaller in non-equilibrium cases due to recombination time of higher ions. The dashed lines show results for higher resolution simulations – $\times 2$ in *NSRDC* and $\times 1.5$ in *CIE* case. It shows that N^+ is roughly converged but N^{2+} and N^{4+} are not-converged at $t_{\text{cool}} \lesssim t \lesssim 200$ kyr (shock velocity $100 \lesssim v_s \lesssim 50 \text{ km s}^{-1}$). This is due to the un-converged temperature structure of the bubble. The dotted line shows a controlled experiment (*NSRDC-X-0.001*) to achieve converged bubble structure.

the recombination rate is a steep function of temperature in this regime.

We conclude that line emissions from high ions such as N^{4+} in the ST phase are expected to trace underionized gas (due to the ionization time of $N^{3+} \rightarrow N^{4+}$), and indicative of non-equilibrium effects. Similarly observing overionized line emission after $t \sim t_{\text{cool}}$ would be a definitive probe of non-equilibrium physics inside the bubble (due to the long recombination time of $N^{6+} \rightarrow N^{5+} \rightarrow N^{4+}$).

4.1.3 Numerical convergence

We check the convergence of the ion column densities for the *CIE* and *NSRDC* cases only. Since the *NSRDC* model has the largest number of physical ingredients included, we plan to compare its column densities with both SSMs and the *CIE* case. The dashed lines in Fig. 9 show higher resolution simulations with resolutions $\times 2$ for the *NSRDC* case and $\times 1.5$ for the *CIE* case. Although N^+ seems converged, N^{2+} and N^{4+} are clearly not converged between $t_{\text{cool}} \lesssim t \lesssim 200$ kyr. The main reason is the slightly different temperature values in the bubble at different resolutions and the unresolved bubble-shell interface. Since both N^{2+} and N^{4+} are produced either in the interface or the bubble (and because $x_{N^{4+}}$ is highly dependent on the bubble temperature), these columns remain sensitive to the resolution.

Although the non-convergence of the bubble and the bubble-shell interface appear unrelated, the bubble is in fact affected by the property of the interface. To clarify this statement, let us examine the density and temperature structures of the region near the interface. We do this for the *NSRDC* case at $t = 150$ kyr, where both $N_{N^{2+}}$ and $N_{N^{4+}}$ seem to be un-converged. This is shown in Fig. 10 where the density is shown in red, temperature in blue, bolometric luminosity, $\mathcal{L}(< r)$ in brown, and the N^{2+} column in green. The solid lines show the values for $\Delta x = 10^{-3}$ pc and the dashed lines show the results for $\Delta x = 5 \times 10^{-4}$ pc resolution. Clearly, the density and temperature of the bubble are not converged. This is very apparent close to the interface that is marked by the grey vertical line. The main reason for this non-convergence is the un-converged cooling at the interface.

Radiative cooling at the interface causes the local plasma to lose its thermal support thereby accumulating on to the shell. Therefore, higher cooling at the interface leads to higher mass accumulation rate from the bubble to the shell which in turn means that the bubble becomes less dense. The lower panel of Fig. 10 shows that the jump in the bolometric luminosity, $\mathcal{L}(< r)$ is smaller at higher resolution, meaning that the interface undergoes less cooling at higher resolution owing to a thinner interface region. This also affects the total energy radiated by the remnant as can be seen in Fig. A1.

Ideally, for an infinite resolution we would be able to resolve the thickness of the interface (field length is $\sim 3 \times 10^{-6}$ pc), which, compared with our resolution element, is very small. This implies negligible cooling loss at the interface and negligible mass accumulation from the bubble to the shell. This would thus allow the bubble to conserve its mass. Since the simulations performed here are computationally expensive, we do not perform even higher resolution simulations. Instead, we perform normal resolution *NSRDC* simulations, but artificially turn-off radiative cooling at the interface⁹ while allowing the ionization network to operate normally. The prescription is only used at $t \geq 60$ kyr (SP phase) when the bubble-shell interface becomes apparent. We call this series of simulations as *NSRDC-X* (*NSRDC-experimental*).

The results for the *NSRDC-X* simulations are also shown in Fig. 10 by the dotted ($\Delta x = 0.0015$ pc) and dot-dashed ($\Delta x = 0.001$ pc) lines. The fact that these two lines are hardly distinguishable in the bubble region shows the success of this experiment. The result is also intuitive. In the absence of any mass accumulation from the bubble to the shell, the bubble now contains the maximum amount of mass possible after the rapid cooling phase. Since the bubble pressure is only a function of time, the temperature of the bubble at

⁹We define the interface ($r_{\text{interface}}$) to be the first instance encountered where the density $> 5n_0$ while going out radially from the centre. The zone, where the cooling is prevented, is defined to be the region that lies within $r_{\text{interface}} \pm 4\Delta x$. Here, Δx is the resolution of that particular simulation.

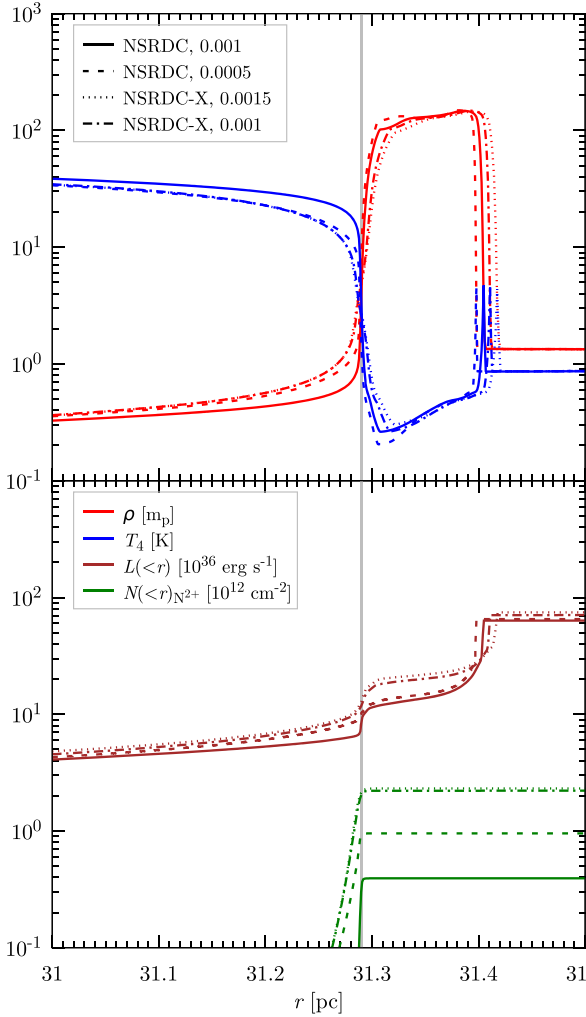


Figure 10. Checking numerical convergence with controlled experiment on *NSRDC*. The figure shows density (red), temperature (blue), cumulative bolometric luminosity (brown), and cumulative N^{2+} column density at $t = 150$ kyr. The solid lines represent *NSRDC* ($\Delta x = 0.001$ pc), the dashed lines show higher resolution version of *NSRDC*, the dotted lines represent results from *NSRDC-X*, $\Delta x = 0.0015$ pc and the dot-dashed line represent results from *NSRDC-X* with $\Delta x = 0.001$ pc. We have adjusted the structures in r -direction slightly (~ 0.02 pc) so that the interfaces of all the runs match at a given location for better visibility. The fact that the dotted and dot-dashed lines are hardly distinguishable in the bubble region indicates excellent convergence in the *NSRDC-X* case.

any given time is now the lowest possible. The N^{2+} column density in the bottom panel (green dotted and dot-dashed lines) also show the convergence for the experimental runs.

Our zero cooling prescription at the interface leads to an artificial density and temperature profile that may differ from the hypothetical infinite resolution simulation. Therefore, any contribution towards the ion column density from the interface region is poorly represented. We present the column densities of the *NSRDC-X*-0.001 pc in Fig. 9 after subtracting the contribution from the interface. Although we do not show the *NSRDC-X*-0.0015 pc column densities to avoid overcrowding, we verified that they are converged (as implied by Fig. 10 too).

In the following comparison of our data to the steady state shocks, we quote the *NSRDC-X*-0.001 pc results.

4.1.4 Comparison with steady-state models

The evolution of the important ion stages for each species (except Mg) for the *NSRDC-X*-p001 case is shown in Fig. 11. Each panel is for a different element, and the curves show the time evolution for each ion of individual elements. The evolution is shown as a function of time rather than velocity since a large part of the evolution is not in steady state. In fact, near $t \sim t_{\text{cool}}$ the velocity is double valued since the shell stops temporarily due to the lack of thermal pressure in the shock but restarts its journey once the hot bubble starts expanding. However, conversion to instantaneous velocity can be easily done using the time-velocity plot shown in the bottom-right panel. Fig. 11 shows that the metal ions are dominated by the neutral or first ionization stages present either in the thin shell or in the background. The flat behaviour for the lower ions like C^0 , C^+ , Si^0 , Si^+ , S^0 , and S^+ reflects the fact that they are produced mostly in the background (region outside the H-ionization front). The sudden fall of atomic column density of C^0 , Si^0 , and S^0 is due to the photoionization caused during the rapid cooling phase ($t_{\text{cool,onset}} \lesssim t \lesssim t_{\text{cool,end}}$).¹⁰ As explained earlier, this is also the reason why the column densities of the next ionization level for these elements are higher at this time. After the rapid cooling phase is over, the singly ionized atoms recombine according to their corresponding recombination rate coefficients and the local electron density. For example, the recombination time-scale for $N^+ \rightarrow C^0$ is $t_{\text{rec},C^+} \sim 1/(n_e \alpha_{C^+}) \approx 40/n_e$ kyr, assuming $\alpha_{C^+} \approx 8 \times 10^{-13} \text{ s}^{-1} \text{ cm}^3$ at $T = 10^4$ K. This means that N^+ can recombine at a time-scale of ~ 40 kyr within the hydrogen IF where $n_e \sim 1$ which is also seen in the increasing column density of C^0 until ~ 130 kyr when the shock reaches the H-ionization front. At larger radii, carbon mostly remains singly ionized since $t_{\text{rec},C^+} \gtrsim \text{Myr}$ owing to the very low value of electron density ($n_e \lesssim 10^{-2}$, given H is mostly neutral at this region).

We also compare our results with steady-state shock calculations. We use the steady state, plane-parallel shock models presented in Gnat & Sternberg (2009) that contain self-consistent radiation field but re-run their models for lower velocities ($\sim 40\text{--}150 \text{ km s}^{-1}$) where the SN remnant spends most of its lifetime. The resulting comparison is shown in Fig. 11. The coloured points show the column densities estimated from the models of Gnat & Sternberg (2009) at ‘given shock velocities’ but converted to ‘given times’ by using the time-velocity curve of the simulated SN shock. Clearly, the shock velocities used for steady-state shock calculations are only achieved for a very short duration of time in a realistic SN shock and therefore it does not get enough time to set up a structure similar to a steady-state structure that makes the comparison a bit unfair. However, since many of the SN studies consider such SSMs to infer either the velocity or the metallicity of the ISM (e.g. Dopita et al. 1980) it is worthwhile to compare these two cases.

Fig. 11 shows that the SSM column density estimates for the lower ions like N^+ , O^+ , O^{2+} , etc. can be off by almost an order of magnitude at $t \lesssim 130$ kyr ($v_s \gtrsim 70 \text{ km s}^{-1}$) in the presence of a recombining precursor. At later times, this discrepancy comes down to only a factor of ~ 5 . The discrepancy is even higher for intermediate and higher ions like N^{2+} , N^{4+} , O^{5+} where the simulated results are almost 2 orders magnitude higher than the expected values from SSMs. Such

¹⁰Note that the IF for C and S extends beyond our computational box of 50 pc. In addition, elements like Mg, Si, Fe are already singly ionized by the assumption of our initial condition at $T = 10^4$ K. Therefore, the column density of N^+ , Mg^+ , S^+ , and Fe^+ are only a lower limit as it depends on the box size.

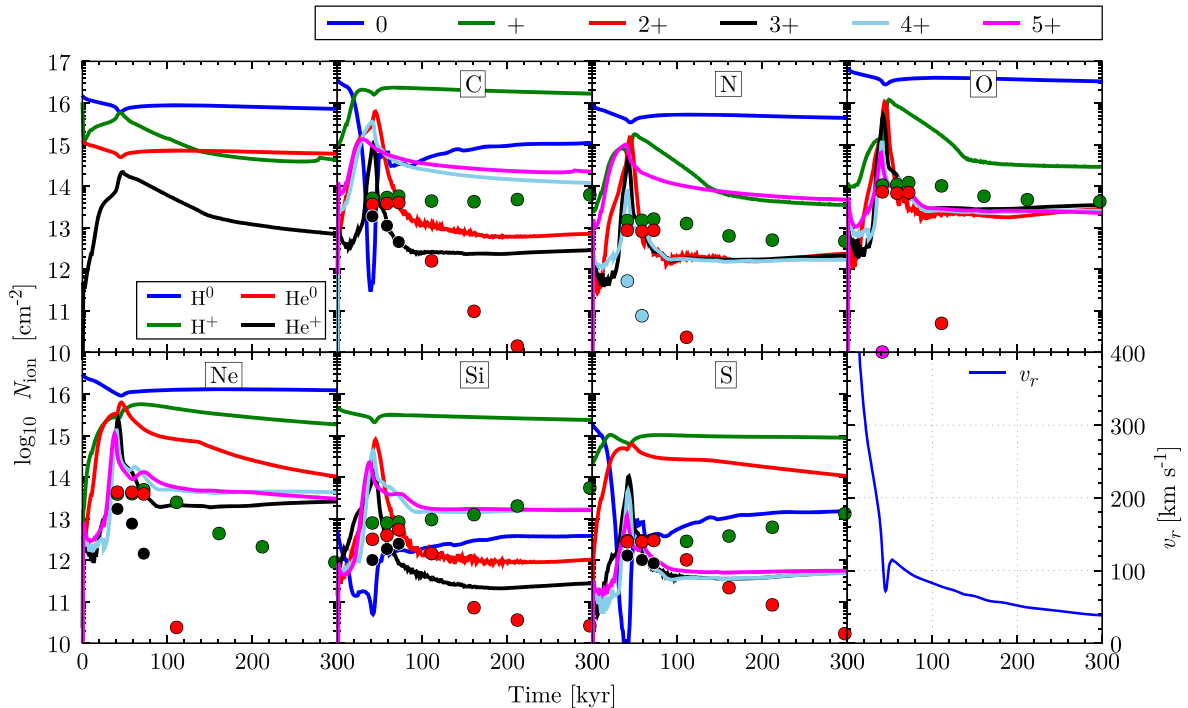


Figure 11. Time evolution of different ion column densities (integrated till the shock front) in the case of NSRDC ($n_{\text{H}} = 1.0 \text{ cm}^{-3}$). Different panels show different species, whereas different lines in each panel represent ions of that species. The top-left panel shows H and He column densities after dividing by 10^4 to bring them to the same scale as others. The small break at $t = 60 \text{ kyr}$ is due to the subtraction of contribution from bubble-shell interface. The bottom-right panel plots the shock velocity with time for reference. Machine readable table containing the simulated column density can be found in the online version.

a severe underestimation of these ions in SSMs is simply due to the fact that the SSMs do not have a hot/warm bubble where most of these ions are produced. A slightly better agreement for the lower ions is expected since the SSMs are roughly able to capture the evolution of density, temperature, and ion fractions just behind the shock where a good fraction of these ions are produced. We conclude from this part that the column densities obtained for an SN remnant using SSMs do not represent the observable column densities.

4.2 Emission spectra

In Fig. 12, we present emission spectra at different times for the NSRDC run. We computed the spectra with high resolution (HR) radiative transfer using the methodology described in paper-I. We include a total of 3457 frequency bins ranging from 10^{13} Hz ($30 \text{ }\mu\text{m}$) to 10^{18} Hz ($3 \text{ }\text{\AA}$) with a frequency resolution $\mathcal{R} = \Delta\nu/\nu \approx 298$. Opacities and emissivities are obtained from CLOUDY-17.01 at each individual radius given the local density, temperature, and non-equilibrium ion fractions of the cell. Although we solve the on-the-fly radiative transfer using only 16 rays ($-1 \leq \mu \leq +1$), we employ a total of 128 rays for our HR computation. The large number of rays allows us to probe the spectra at different impact parameters across the SN remnant. The impact parameters (b) are simply converted from the μ values at that radius since $b = r \sin \theta = r \sqrt{1 - \mu^2}$. We calculate the spectra at the edge of the simulation box assuming that any additional emission or absorption by the foreground medium can be calculated easily.

We show the resulting spectra for $b = 0$ in Fig. 12 for three different times representing different phases of the SN remnant. Typical emission from a plasma in our case consists of the free-free

emission (Bremsstrahlung), the free-bound emission (continuum emissions from recombination of free electrons on to ions, and the bound-bound transition (mostly line emissions, but can also be continuum emission in special cases). The absorption is mostly from the Ly-continuum and different metal-lines. As can be seen in the left-hand panel of the figure, the X-ray emission at $\lambda \lesssim 100 \text{ }\text{\AA}$ is due to the Bremsstrahlung emission from hot plasma at the shock front and almost vanishes at later times when the shell is much cooler. The dip in the spectra around $\lambda \sim 100\text{--}912 \text{ }\text{\AA}$ is due to the Ly-continuum absorption by the neutral hydrogen present in the region between the shock front to the edge of the simulation box. The bright emission lines immediately after $\lambda = 912 \text{ }\text{\AA}$ are the Ly- δ , Ly- γ , Ly- β lines from recombining hydrogen plasma. Another bright peak clearly seen at $1216 \text{ }\text{\AA}$ is the Ly- α emission line. Note that the actual line brightness and the line shape of the Ly- α line may be different than obtained here since this is a highly resonant line and it diffuses both in space and frequency that are not modelled in our radiative transfer algorithm. The continuum emission right after $\lambda \geq 1216 \text{ }\text{\AA}$ is the two photon emission from hydrogen $2s \rightarrow 1s$ level (since a single photon emission is forbidden between these two levels).

We show a zoomed in view of the spectra in the right-hand panel of Fig. 12 in the UV frequency range that can be probed by HST COS or other spectrographs. We find that emissions from higher ions like O IV, O VI, N IV, N V are only present at earlier time ($\lesssim 40 \text{ kyr}$) when the shock temperature is higher. The lines are brighter at $t \approx 40 \text{ kyr}$ since the temperature of the shell is $\sim 10^5 \text{ K}$, suitable to produce these ions. At later times ($t \gtrsim 80 \text{ kyr}$), emission from the lower ions like C II, Mg II, etc. prevail. As can be seen in the left-hand panel that the SN remnant becomes much brighter in optical bands ($\sim 4000\text{--}7000 \text{ }\text{\AA}$) at later times as the shock slows down.

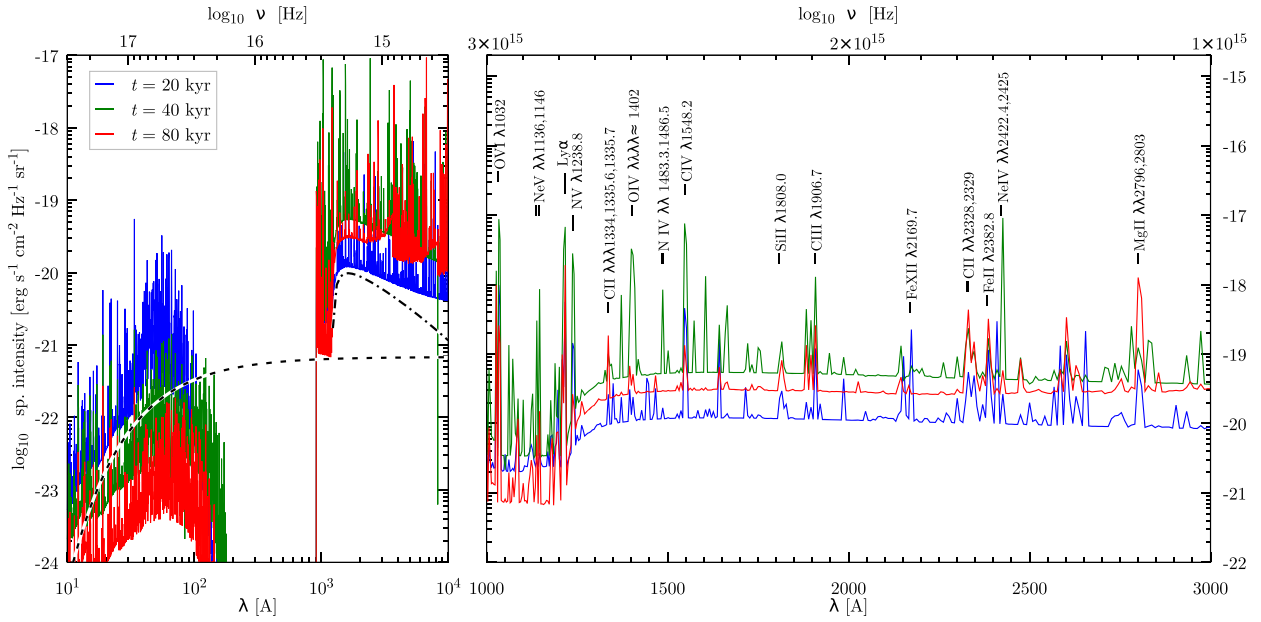


Figure 12. Emission spectra at $t = 20$ kyr (blue), $t = 40$ kyr (green), and $t = 80$ kyr (red) for the NSRDC run at zero impact parameter. The spectra are obtained by performing full radiative transfer till the edge of the simulation box, i.e. 50 pc. The left-hand panel shows the full spectra from 10 to 10 000 Å, whereas the right-hand panel shows a zoomed in version of it to indicate a few possible emission lines. The dashed black line in the left-hand panel shows arbitrarily scaled Bremsstrahlung emission from $T = 2 \times 10^6$ K plasma (Draine 2011) and the dot-dashed black line shows arbitrarily scaled two-photon emission spectra (Nussbaumer & Schmutz 1984) for comparison.

5 DISCUSSION

In this paper, we have studied the effects of NEI and associated cooling, radiative transfer, and thermal conduction on the structures and chemical states of expanding SN blast wave shells. There are several physical, numerical as well as methodological aspects that we have not included so far. We discuss them here.

5.1 3D versus 1D

One important difference between our simulations and real SNRs is our assumption of spherical symmetry. It is well known that a thin shell driven by thermal pressure of the interior gas is subject to shell instabilities such as the Vishniac instability (Vishniac 1983) when the assumption of spherical symmetry is dropped and the shock is radiative enough so that the effective adiabatic index is ≤ 1.1 . This instability arises even if the shock is moving into an initially uniform background. It occurs because the hot gas pressure acts normally to the surface, whereas ram pressure on the shell presses radially inwards. This causes the shell to have a net force along the non-radial directions and any small deformation of the spherical shell results in filamentary structures and finally fragmentation (Krause et al. 2013; Steinberg & Metzger 2018). Therefore, a full 3D or at least a 2D simulation may produce significant clumping of the shell, thereby breaking the spherical symmetry. Such clumping may increase the dust opacity in the shell by reducing the dust destruction. Steinberg & Metzger (2018) have shown that the average shock temperature where most of the cooling occurs may also change due to such clumping. The average shock radius, however, does not seem to vary much compared to a 1D calculation (Krause et al. 2013; Yadav et al. 2017). However, analysis of laboratory shocks (Grun et al. 1991;

Laming & Grun 2002, 2003) suggests that atomic shocks in cosmic abundance plasma are unlikely to be sufficiently radiative.

In addition to the 3D instabilities, pure 1D instabilities, such as oscillatory instability also may arise in the thin shell (Chevalier & Imamura 1982). It is expected that the radiative shocks, following a cooling function $\Lambda(T) \propto T^\alpha$, are generally stable against the 1D oscillatory instability if $\alpha > \alpha_{\text{cr}} = 3$. Although later works show that this critical exponent, α_{cr} , is dependent on the Mach number of the shock and whether the shock needs to cool down only to the level of the pre-shocked material or not (Laming 2004; Pittard et al. 2005). These authors show that for $\alpha = 3$, the radiative shock becomes unstable only at Mach $\gtrsim 10$. With lower Mach numbers, the α_{cr} decreases. Pittard et al. (2005) show that for Mach = 5, $\alpha_{\text{cr}} = -0.4$ at least for the first overtone (which contains most of the power) and the system becomes stable against the oscillatory instability. Given that a roughly steady radiative shock only appears in our simulations at $t \gtrsim 60$ kyr i.e. $v_s \lesssim 110$ km s $^{-1}$ (Mach $\lesssim 10$), Fig. 5 suggests that $\alpha \gtrsim 2$ at this velocity range. Therefore, we speculate that in the case presented here, the radiative shock is mostly stable against the 1D oscillatory instabilities. However, a definite answer to the question may be difficult to provide in our current simulation set-up since we do not impose any perturbations on the expanding shell. Besides, the cooling layer behind the shock may not be well resolved due to our numerical resolution.

Throughout our simulations, we have assumed that the background material is uniform in density and pressure owing to the uniform temperature. In reality, the ISM density is often non-uniform and much of the pressure comes from the non-thermal components, like turbulence. For example, the typical turbulence speed in the Milky Way ISM is about ~ 15 – 20 km s $^{-1}$ (Krumholz, Kruijssen & Crocker 2017) compared to the adiabatic sound speed of ≈ 15 km s $^{-1}$

(assuming $T = 10^4$ K). Clearly, the turbulent structure in the ISM is non-negligible. This can further amplify fragmentation.

5.2 Mixing layer prescriptions

As we explained in Section 4.1.3, the formation of ions such as N^{2+} and N^{4+} is heavily dependent on the bubble properties that depend on the exact amount of cooling and accumulation of gas at the bubble-shell interface. The interface itself is a significant source of ions like N^{2+} , O^{2+} , etc. The 3D instabilities in the interface region therefore can substantially change these ion columns. Addressing this issue is out of the scope of this paper. One thing that we could do in the current simulation is to use a mixing layer prescription (e.g. Duffell 2016) as used by El-Badry et al. (2019). We, however, must note that the validity of these prescriptions is verified only in controlled cases, and only in terms of the average density and temperature profiles. Given that the total cooling and ion columns strongly depend on the local density, temperature, and the evolution history, a traditional mixing layer prescription seems insufficient and may even lead to completely wrong column densities. We therefore do not use (or plan to use) a mixing layer prescription in our work.

5.3 Magnetic field

In our study of the effects of NEI/recombination with the self-radiation, we have not included any magnetic field (MF; B). Slavin & Cox (1992) found that for an SN remnant expanding into a medium with $n_H = 0.2 \text{ cm}^{-3}$ an MF suppresses the density jump behind the shock and depends on the exact strength of the field. The shock radius seems to grow faster at $t \gtrsim 1$ Myr. In a recent simulation, Evirgen & Gent (2019) showed that for an SN into a $n_H = 1 \text{ cm}^{-3}$ medium, the shock radius depends on the direction of the MF. For a shock moving perpendicular to the field, the difference can be only ~ 5 per cent at $t \approx 400$ kyr (for $B = 5 \mu\text{G}$), whereas the shock radius does not change much if the shock moves parallel to the field direction. They also showed that the residual net energy (both kinetic and thermal) only increases by a factor of 20 per cent compared to no MF cases after the end of 500 kyr. We therefore do not expect any dramatic changes in the dynamics of the SN remnant simulated here.

The column densities and emission spectra are, however, expected to change due to the presence of the MF (Gnat & Sternberg 2009; Petruk, Kuzyo & Beshley 2016; Bach 2019). The density and pressure profiles behind the shock can be altered during the rapid cooling phase (their fig. 4). This may cause a lower radiation in high field strengths. Since the precursor region in our simulation depends on the radiation from the rapid cooling phase, we expect this region to be smaller for increasing MF. Petruk et al. (2016) also showed that the suppression in density jump behind the shock leads to an increased shock temperature in general. Since both the cooling function behind the shock and the recombination rates are dependent on the actual density, non-equilibrium ion fractions and local radiation field in a non-trivial manner (Fig. 5), it is hard to speculate the exact outcome of the MF on the column densities and emerging spectra. We therefore keep this task for future work.

In addition to the direct effects of the MF on the shock, a shock running through a magnetized ambient medium may also accelerate particles and plasma waves that may radiate away thermal energy of the shock via non-thermal channels (Edmiston & Kennel 1984; Quest 1988; Laming 2001; Treumann 2009). Therefore, this process can make the shock prone to instabilities (discussed in previous sections) by increasing cooling. It is also possible that the particle

acceleration and plasma waves can amplify the MF upstream, thereby increasing the stability of the shock against the above mentioned instabilities. One needs to perform full MHD simulations (preferably using ‘particle-in-cell method’) along with NEI and radiative transfer to properly answer these questions.

5.4 Dust grain size

In our computations, we make the simplifying approximation that the dust extinction cross-section is proportional to the area of a typical dust grain of initial size $a = 0.1 \mu\text{m}$. We do not consider a grain size distribution. The effect of dust is, however, expected to change our results only for the high density runs as we discussed in paper-I. The critical density above which dust affects the size of a Strömgren sphere is $n_{\text{crit}} \sim 100 Q_{49}^{-1} T_4^{-0.84} \sigma_{\text{ext}, -21}^{-3}$ (see paper-I), where Q_{49} is the ionizing photon luminosity in 10^{49} photons s^{-1} , $T_4 = T/10^4 \text{ K}$ is the temperature of the ionized sphere and $\sigma_{\text{ext}, -21} = \sigma_{\text{ext}}/10^{-21}$ is the extinction cross-section of the dust particles. Given the standard values for our SN shock and its precursor during the rapid cooling phases (see Section 3.4), we estimate this value to be $n_{\text{crit}} \approx 100 \text{ cm}^{-3}$. We therefore do not expect any change in the precursor region due to dust. The formation of a dense shell ($n_H \sim 100 \text{ cm}^{-3}$) may seem to affect the radiative transfer through the shell. However, by the time such a dense shell forms, the H^0 fraction also increases inside the shell so that the H^0 opacity dominates over the dust extinction. We therefore do not expect too much change in the radiative transfer through the dense shell either. We assess that the effect of dust may be important in the SNRs exploding inside denser media ($n_H \gtrsim 100 \text{ cm}^{-3}$).

5.5 Progenitor O/B star

Another possible limitation of our current calculation is the absence of any pre-perturbed medium (e.g. perturbations by the progenitor star) in which the SN explodes. For example, for a progenitor star of class O7-III (mass $= 47.4 M_\odot$), the mass-loss rate (\dot{M}_*), and H^0 ionizing photon luminosities are $\approx 3 \times 10^{-6} M_\odot \text{ yr}^{-1}$ and 2×10^{49} photon s^{-1} , respectively, for the initial 3 Myr before the SN goes off (Sternberg, Hoffmann & Pauldrach 2003). Given such a large UV luminosity, the star is expected to set up a Strömgren’s sphere out to a radius of $\approx 86 \text{ pc}$ (for $n_H = 1 \text{ cm}^{-3}$) within the first $t_{\text{rec}} \sim 1/n_H \alpha(T) \sim 120$ kyr of its evolution. In this context, it is interesting to note that while many core-collapse SNe indeed likely completely ionize their circumstellar medium before exploding or as they explode, SNe Ia seem to explode into at least partially neutral material, as is evident by their Ly α emission (e.g. Ghavamian et al. 2007). While the ionizing radiation is not expected to change the density inside the ionized sphere by much (see paper-I), the stellar wind from the star can change the density distribution to a large extent. The mechanical luminosity injected by such a star is $\frac{1}{2} \dot{M}_* v_w^2 \approx 5.5 \times 10^{36} \text{ erg s}^{-1}$, considering the wind velocity $v_w \approx 2400 \text{ km s}^{-1}$ (Sternberg et al. 2003). The corresponding bubble will sweep out the gas to a thin shell at a distance of $\approx 63 \text{ pc}$ after 3 Myr (when the star presumably goes off as SN) of its evolution inside a $n_H = 1 \text{ cm}^{-3}$ medium (Castor, Weaver & McCray 1975; Weaver et al. 1977). This is clearly, larger than the shock radius from the SN within first 500 kyr. Therefore, the SN will explode in a region with density much lower than 1 cm^{-3} and the SN energy will be quickly redistributed to the already existing shell created by the stellar wind. The evolution of the SN shock across the shell is complex given that the shock now travels through an already collapsed high density

and non-uniform shell whose density structure can be only found via simulations.

6 SUMMARY

We have performed simulations of a spherically symmetric expanding SN remnant up to 500 kyr into an initially uniform background medium with hydrogen density, $n_0 = 1 \text{ cm}^{-3}$. We consider NEI network, conduction, frequency dependent radiative transport, and simple dust effects in addition to the usual hydrodynamics. The self-consistent treatment of these processes has lead us to obtain very detailed understanding of the SN remnant evolution, many aspects for the first time. Our understanding of the remnant evolution can be summarized as follows:

(i) We find that the presence of complex physics like the dynamically evolving ion network, conduction, and radiative transport does not alter the dynamics or energetics of the remnant compared to a simple model in which collisional ionization equilibrium is assumed. Therefore, the thermal energy and momentum feedback from the SN to the ISM is not significantly affected by the inclusion of more detailed processes including the complex physics of NEI, radiative transfer, or conduction (ref Fig. 4).

(ii) The cooling function of the material behind the shock (down to the outer radius of the hot bubble) does not follow any particular known cooling function throughout its evolution. Rather, it goes through a mixture of them. At earlier times ($t < t_{\text{cool,onset}}$), the cooling follows simple CIE cooling due to high enough temperature ($T \gtrsim 10^6 \text{ K}$) at the shock. During the rapid cooling phase ($t_{\text{cool,onset}} \lesssim t \lesssim t_{\text{cool,end}}$), the cooling function follows a simple isochoric cooling of a photoionized plasma due to the presence of a large number of H^0 ionizing photons at this phase. In the SP phase ($t \gtrsim t_{\text{cool,end}}$), the cooling function is enhanced by more than an order of magnitude compared to a simple CIE model due to the presence of different ions that are out of equilibrium (ref Fig. 5).

(iii) The cooling shell during the rapid cooling phase, can be as bright as an O star in terms of its UV luminosity but only for ≈ 20 kyr. This sets a precursor region up to ~ 10 pc ahead of the shock (for $n_{\text{H}} = 1 \text{ cm}^{-3}$). This precursor region does not expand further with time but the ions inside this region recombine to produce a precursor region that decreases with time. The ionization level inside the precursor region is therefore not a direct function of the velocity as in the steady state, plane-parallel shock models, rather it depends on the recombination time of the ions. Although the precursor region persists ahead of the shock until $v_s \lesssim 70 \text{ km s}^{-1}$, consistent with the plane-parallel, steady-state shock, the reason behind it is different (ref Fig. 7).

(iv) The presence of ions like C^{3+} , N^{4+} , O^{5+} , etc. in excess of 10^{14} cm^{-2} (for $n_0 = 1.0 \text{ cm}^{-3}$) implies that the SN remnant is undergoing a rapid cooling phase. These ions are expected to remain overionized inside the bubble due to delayed recombination.

(v) The observable column densities for different ions can differ by a factor between 5 and a few orders of magnitude compared to estimations from plane-parallel steady-state shocks (Fig. 11). Major differences are (i) the non-steady behaviour of the shock, (ii) the geometrical factors, and (iii) the non-steady precursor. Such fundamental drawbacks of the steady-state shock models lead to severe underestimation of the presence of many ions and should be used cautiously.

In conclusion, despite several limitations of the simulations performed in this paper, we believe that we have been able to understand some fundamental aspects of the radiative transport and

non-equilibrium ion dynamics in an SN remnant and a spherical shock, in general. Challenges, however, remain to deal with the limitations of spherical symmetry, MF, and initial density distribution due to the progenitor star. We hope to address them in our future works.

ACKNOWLEDGEMENTS

We acknowledge the helpful discussion by Yakov Faerman and Eve Ostriker. We thank the Center for Computational Astrophysics (CCA) at the Flatiron Institute Simons Foundation for hospitality and for computational support via the Scientific Computing Core. We also thank the anonymous referee for his/her comments that improved the content of this paper. This work was supported by the German Science Foundation via DFG/DIP grant STE 1869/2-1 GE625/17-1 at Tel Aviv University, the Israeli Centers of Excellence (I-CORE) program (centre no. 1829/12) and the Israeli Science Foundation (ISF grant no. 2190/20).

DATA AVAILABILITY

The data underlying this article are available in the article and in its online supplementary material.

REFERENCES

- Bach J. B., 2019, PhD thesis, Hebrew University of Jerusalem
 Becker R. H., Holt S. S., Smith B. W., White N. E., Boldt E. A., 1980, *ApJ*, 235, 5
 Breitschwerdt D., de Avillez M. A., 2006, *A&A*, 452, L1
 Castor J., Weaver R., McCray R., 1975, *ApJ*, 200, L107
 Chevalier R. A., Imamura J. N., 1982, *ApJ*, 261, 543
 Cioffi D. F., McKee C. F., Bertschinger E., 1988, *ApJ*, 334, 252
 Cowie L. L., McKee C. F., 1977, *ApJ*, 211, 135
 Cox D. P., 1972a, *ApJ*, 178, 143
 Cox D. P., 1972b, *ApJ*, 178, 159
 Cox D. P., 2005, *ARA&A*, 43, 337
 Cox D. P., Anderson P. R., 1982, *ApJ*, 253, 268
 Cui W., Cox D. P., 1992, *ApJ*, 401, 206
 De Avillez M. A., Breitschwerdt D., 2012, *ApJ*, 761, L6
 de Avillez M. A., Mac Low M.-M., 2002, *ApJ*, 581, 1047
 Dekel A., Silk J., 1986, *ApJ*, 303, 39
 Dekel A., Sarkar K. C., Jiang F., Bournaud F., Krumholz M. R., Ceverino D., Primack J. R., 2019, *MNRAS*, 488, 4753
 Dopita M. A., 1976, *ApJ*, 209, 395
 Dopita M. A., Sutherland R. S., 1996, *ApJS*, 102, 161
 Dopita M. A., Dodorico S., Benvenuti P., 1980, *ApJ*, 236, 628
 Dopita M. A., Seitzzahl I. R., Sutherland R. S., Nicholls D. C., Vogt F. P. A., Ghavamian P., Ruiter A. J., 2019, *AJ*, 157, 50
 Draine B. T., 2011, *Physics of the Interstellar and Intergalactic Medium*. Princeton Univ. Press, Princeton, NJ
 Duffell P. C., 2016, *ApJ*, 821, 76
 Edmiston J. P., Kennel C. F., 1984, *J. Plasma Phys.*, 32, 429
 El-Badry K., Ostriker E. C., Kim C.-G., Quataert E., Weisz D. R., 2019, *MNRAS*, 490, 1961
 Evirgen C. C., Gent F., 2019, preprint ([arXiv:1908.08781](https://arxiv.org/abs/1908.08781))
 Fesen R. A., Kirshner R. P., 1980, *ApJ*, 242, 1023
 Fesen R. A., Blair W. P., Kirshner R. P., 1985, *ApJ*, 292, 29
 Ghavamian P., Laming J. M., Rakowski C. E., 2007, *ApJ*, 654, L69
 Gnat O., 2017, *ApJS*, 228, 1
 Gnat O., Sternberg A., 2007, *ApJS*, 168, 213
 Gnat O., Sternberg A., 2009, *ApJ*, 693, 1514
 Grun J., Stamper J., Manka C., Resnick J., Burris R., Crawford J., Ripin B. H., 1991, *Phys. Rev. Lett.*, 66, 2738
 Haardt F., Madau P., 2012, *ApJ*, 746, 125

- Hamilton A. J. S., Sarazin C. L., Chevalier R. A., 1983, *ApJS*, 51, 115
- Itoh H., 1978, *PASJ*, 30, 489
- Kafatos M., 1973, *ApJ*, 182, 433
- Kewley L. J., Dopita M. A., Sutherland R. S., Heisler C. A., Trevena J., 2001, *ApJ*, 556, 121
- Kim C. G., Ostriker E. C., 2015, *ApJ*, 802, 1
- Kopsacheili M., Zezas A., Leonidaki I., 2020, *MNRAS*, 491, 889
- Krause M., Fierlinger K., Diehl R., Burkert A., Voss R., Ziegler U., 2013, *A&A*, 550, A49
- Krumholz M. R., Kruijssen J. M. D., Crocker R. M., 2017, *MNRAS*, 466, 1213
- Krumholz M. R., Burkhardt B., Forbes J. C., Crocker R. M., 2018, *MNRAS*, 477, 2716
- Laming J. M., 2001, *ApJ*, 546, 1149
- Laming J. M., 2004, *Phys. Rev. E*, 70, 057402
- Laming J. M., Grun J., 2002, *Phys. Rev. Lett.*, 89, 125002
- Laming J. M., Grun J., 2003, *Phys. Plasmas*, 10, 1614
- Larson R. B., 1974, *MNRAS*, 169, 229
- McKee C. F., Ostriker J. P., 1977, *ApJ*, 218, 148
- Mathewson D. S., Clarke J. N., 1973, *ApJ*, 180, 725
- Mignone A., Bodo G., Massaglia S., Matsakos T., Tesileanu O., Zanni C., Ferrari A., 2007, *ApJS*, 170, 228
- Nath B. B., Trentham N., 1997, *MNRAS*, 291, 505
- Nussbaumer H., Schmutz W., 1984, *A&A*, 138, 495
- Okon H. et al., 2020, *ApJ*, 890, 62
- Petrak O., Kuzyo T., Beshley V., 2016, *MNRAS*, 456, 2343
- Pittard J. M., Dobson M. S., Durisen R. H., Dyson J. E., Hartquist T. W., O'Brien J. T., 2005, *A&A*, 438, 11
- Quest K. B., 1988, *J. Geophys. Res.*, 93, 9649
- Ritchey A. M., 2020, *MNRAS*, 495, 2909
- Ritchey A. M., Jenkins E. B., Federman S. R., Rice J. S., Caprioli D., Wallerstein G., 2020, *MNRAS*, 897, 83
- Sarkar K. C., Sternberg A., Gnat O., 2021, *MNRAS*, preprint (arXiv:2010.00457) (paper-I)
- Shull J. M., McKee C. F., 1979, *ApJ*, 227, 131
- Slavin J. D., Cox D. P., 1992, *ApJ*, 392, 131
- Spitzer L., 1956, *Physics of Fully Ionized Gases*. Dover Press, New York
- Steinberg E., Metzger B. D., 2018, *MNRAS*, 479, 687
- Steinwandel U. P., Moster B. P., Naab T., Hu C.-Y., Walch S., 2020, *MNRAS*, 495, 1035
- Sternberg A., Hoffmann T. L., Pauldrach A. W. A., 2003, *ApJ*, 599, 1333
- Sutherland R. S., Dopita M. A., 2017, *ApJS*, 229, 34 (SD2017)
- Tesileanu O., Mignone A., Massaglia S., 2008, *A&A*, 488, 429
- Treumann R. A., 2009, *A&AR*, 17, 409
- Vasiliev E. O., 2013, *MNRAS*, 431, 638
- Vishniac E. T., 1983, *ApJ*, 274, 152
- Weaver R., McCray R., Castor J., Shapiro P., Moore R., 1977, *ApJ*, 218, 377
- Weingartner J. C., Draine B. T., 2001, *ApJ*, 548, 296
- Yadav N., Mukherjee D., Sharma P., Nath B. B., Mukherjee D., Sharma P., Nath B. B., 2017, *MNRAS*, 465, 1720
- Zhang G.-Y., Foster A., Smith R., 2018, *ApJ*, 864, 79
- Zhang G.-Y., Slavin J. D., Foster A., Smith R. K., Zuhone J. A., Zhou P., Chen Y., 2019, *ApJ*, 875, 81

SUPPORTING INFORMATION

Supplementary data are available at *MNRAS* online.

combined_colden.dat

Please note: Oxford University Press is not responsible for the content or functionality of any supporting materials supplied by the authors. Any queries (other than missing material) should be directed to the corresponding author for the article.

APPENDIX A: ENERGETICS

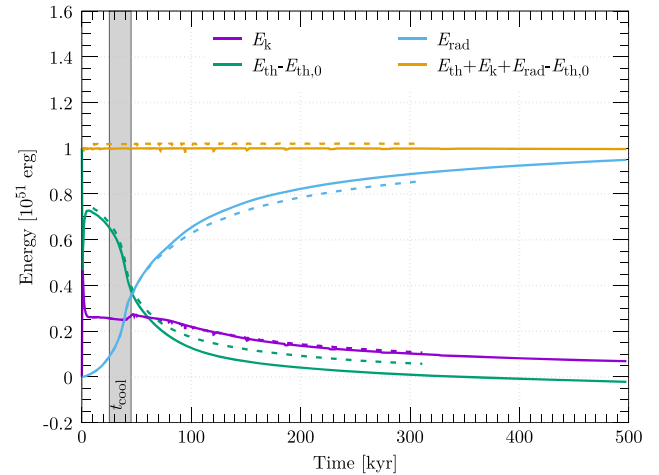


Figure A1. Evolution of energetics of an SN in a $n_{\text{H}} = 1 \text{ cm}^{-3}$ background medium for NSRDC case (dashed line). The solid line shows a simulation with resolution of $\Delta r = 0.0061 \text{ pc}$ and box size of 100 pc comparing the effects of resolution on energetics. Different lines represent different energy components inside the simulation box. The green lines show the internal energy after subtracting the initial thermal energy of the box and the magenta lines show the kinetic energy. The sky-blue lines show the energy that is radiated away from the box, mostly due to the evolution of the SN remnant and a small part from the cooling of the background material. The golden lines show the total energy (kinetic + thermal + radiation loss-initial thermal energy) conservation in the simulation. The extension of the rapid cooling phase is shown by the grey band near 40 kyr. Note that the SN remnant loses almost 30 per cent of its energy during this phase. The energy components flatten after $\sim 300 \text{ kyr}$ and rise only by a few per cent after that. The reduced energy loss in HR simulation is due to reducing artificial cooling at the bubble-shell interface as explained in Section 4.1.3.

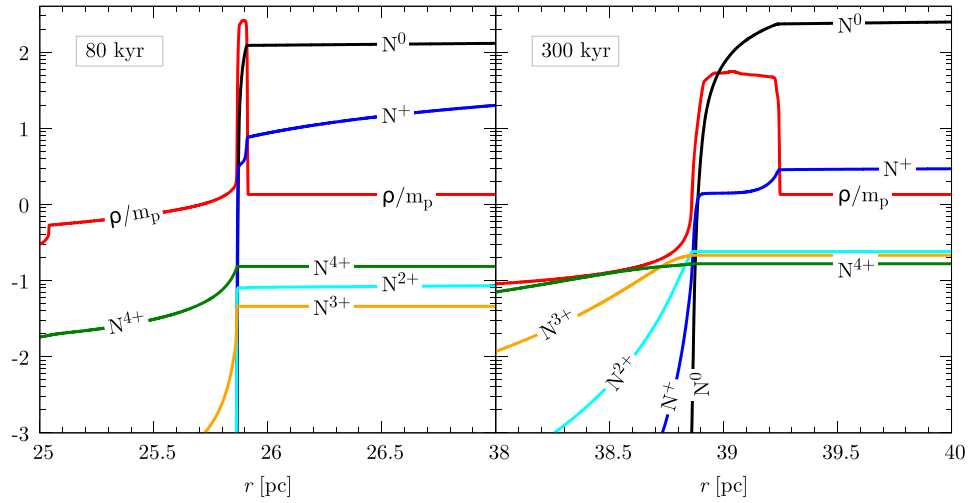


Figure A2. Origin of ions at late stages – when the precursor is present (left column) and when the precursor is not present and the bubble temperature is suitable for the production of higher ions (right column).

This paper has been typeset from a \LaTeX file prepared by the author.